

An Active Site Inhibitor Induces Conformational Penalties for ACE2 Recognition by the Spike Protein of SARS-CoV-2

Billy J. Williams-Noonan, Nevena Todorova, Ketav Kulkarni, Marie-Isabel Aguilar, and Irene Yarovsky*

Cite This: <https://dx.doi.org/10.1021/acs.jpcb.0c11321>

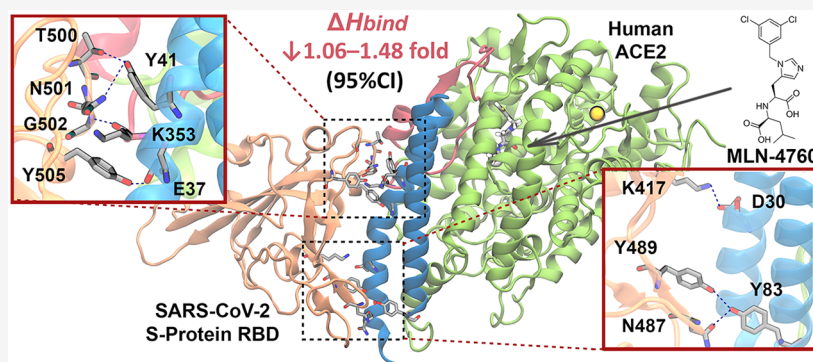
Read Online

ACCESS |

Metrics & More

Article Recommendations

Supporting Information



ABSTRACT: The novel RNA virus, severe acute respiratory syndrome coronavirus II (SARS-CoV-2), is currently the leading cause of mortality in 2020, having led to over 1.6 million deaths and infecting over 75 million people worldwide by December 2020. While vaccination has started and several clinical trials for a number of vaccines are currently underway, there is a pressing need for a cure for those already infected with the virus. Of particular interest in the design of anti-SARS-CoV-2 therapeutics is the human protein angiotensin converting enzyme II (ACE2) to which this virus adheres before entry into the host cell. The SARS-CoV-2 virion binds to cell-surface bound ACE2 via interactions of the spike protein (s-protein) on the viral surface with ACE2. In this paper, we use all-atom molecular dynamics simulations and binding enthalpy calculations to determine the effect that a bound ACE2 active site inhibitor (MLN-4760) would have on the binding affinity of SARS-CoV-2 s-protein with ACE2. Our analysis indicates that the binding enthalpy could be reduced for s-protein adherence to the active site inhibitor-bound ACE2 protein by as much as 1.48-fold as an upper limit. This weakening of binding strength was observed to be due to the destabilization of the interactions between ACE2 residues Glu-35, Glu-37, Tyr-83, Lys-353, and Arg-393 and the SARS-CoV-2 s-protein receptor binding domain (RBD). The conformational changes were shown to lead to weakening of ACE2 interactions with SARS-CoV-2 s-protein, therefore reducing s-protein binding strength. Further, we observed increased conformational lability of the N-terminal helix and a conformational shift of a significant portion of the ACE2 motifs involved in s-protein binding, which may affect the kinetics of the s-protein binding when the small molecule inhibitor is bound to the ACE2 active site. These observations suggest potential new ways for interfering with the SARS-CoV-2 adhesion by modulating ACE2 conformation through distal active site inhibitor binding.

INTRODUCTION

Due to the current global pandemic, there is a clear need for novel drugs targeting severe acute respiratory syndrome coronavirus II (SARS-CoV-2). Considerable effort has been invested into understanding SARS-CoV-2 throughout the early months of 2020,^{1,2} and multiple potential drug targets relevant to SARS-CoV-2 have been reported. Angiotensin converting enzyme II (ACE2) is expressed on the surface of human cells and is a promising target for the rational design of novel anti-SARS-CoV-2 drugs.² Human ACE2 is involved in the renin angiotensin system, which regulates vasoconstriction and blood pressure throughout the body. The native ligand for ACE2 is angiotensin II (AngII), which is a peptide with the sequence DRVYIHPF.^{3–5} A multidomain spike protein (s-protein) on the viral envelope of SARS-CoV-2 interacts with an allosteric

site of ACE2 that is distal to the ACE2 active site. This initial adhesion step where the s-protein binds to ACE2 is followed by viral entry into the host cell. Therefore, both the s-protein and human ACE2 are putative drug targets for the design of anti-SARS-CoV-2 therapeutics.²

The inhibition of the binding of SARS-CoV-2 s-protein to ACE2 would prevent the entry of virions into the cell, and the

Received: December 21, 2020

Revised: January 28, 2021

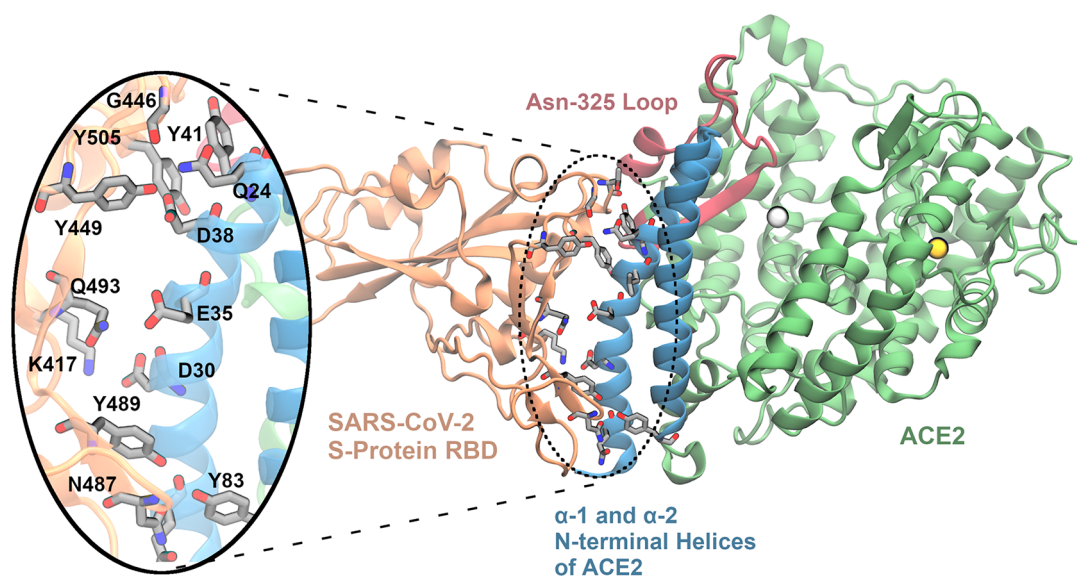


Figure 1. ACE2 with bound viral s-protein RBD from PDB-ID: 6M0J. The ACE2 receptor is shown with a dark green ribbon representation. The ACE2 N-terminal helices starting at Ser-19, which interact with the SARS-CoV-2 s-protein RBD, are shown as blue ribbons, and the adjacent loop starting at Asn-325, which also contains residues that interact with the SARS-CoV-2 s-protein RBD, is colored red. Catalytic zinc and chloride ions are silver and yellow spheres, respectively. The SARS-CoV-2 s-protein RBD is shown in an orange ribbon representation. A close-up view of the key residue interactions between ACE2 and s-protein RBD are shown as sticks. Hydrogens are not shown as they were unresolved by crystallography.

amino acid residues involved in the ACE2/s-protein interaction are central to viral entry. The s-protein has multiple domains, and of interest in this paper is the domain that binds to human ACE2 (the receptor binding domain, RBD). To date, there are three reported crystal structures of the ACE2/SARS-CoV-2 s-protein complex (PDB-IDs: 6M0J, 6LZG, and 6VW1).^{6–8} Several ACE2 and s-protein residues have been identified as part of the ACE2/s-protein interaction by inspection of a crystal structure of the complex.⁶ Using a published crystal structure of the ACE2/s-protein RBD complex (PDB-ID: 6M0J),⁶ we define ACE2 motifs within 6 Å of the viral s-protein RBD in the ACE2 complex as the s-protein binding site of ACE2. An illustration of the ACE2/s-protein RBD complex is shown in Figure 1. The viral s-protein binding site motifs of ACE2 include residues Ser-19 to Tyr-83 (Figure 1, blue ribbons) and the Gln-325 to Asp-355 (Figure 1, red ribbons) protein sequences. Represented as a focused region in Figure 1 are key interacting residues between the N-terminal helices plus the Asn-325 loop of ACE2 (or the s-protein binding site of ACE2) and the SARS-CoV-2 s-protein RBD, as initially depicted in a recent *Nature* publication by Lan et al.⁶

The SARS-CoV-2 s-protein binds to ACE2 with higher affinity than the SARS-CoV s-protein,^{6,9,10} potentially explaining the higher infectivity of SARS-CoV-2 in humans. This improved binding strength with SARS-CoV-2^{6,9,10} is in part explained by several key mutations between the SARS-CoV and SARS-CoV-2 s-protein residues that make interactions with the ACE2 s-protein binding site. Specifically, the residues that differ between SARS-CoV and SARS-CoV-2 s-proteins include: V404 → K417, R426 → N439, Y442 → L455, L443 → F456, L460 → F473, L472 → F486, L479 → Q493, D480 → S456, Y484 → Q498, and T487 → N501.¹¹ These specific mutations result in improved binding strength for the SARS-CoV-2 s-protein, where the dissociation constant (K_D) for SARS-CoV-2 s-protein binding is improved by between 3- and 4-fold compared to the equivalent K_D for SARS-CoV s-protein

binding.⁶ This improvement in the K_D of SARS-CoV/SARS-CoV-2 s-protein binding may be as high as 20-fold,⁹ and the exact magnitude of the difference could depend on the specific methods used to measure K_D .⁶ Walls et al.¹⁰ report an approximately 4.2-fold improvement in K_D between SARS-CoV and SARS-CoV-2 s-proteins and ACE2 but suggested that this small improvement in the initial adhesion event for SARS-CoV-2 was not the cause of increased infectivity. They report that the conformational flexibility of the s-protein RBD of SARS-CoV-2 would affect the feasibility of the subsequent viral membrane-fusion event and that this would have a greater effect on the improved infectivity of SARS-CoV-2.¹⁰ The consensus so far appears to be that the marginal difference in binding strength between ACE2 and SARS-CoV/SARS-CoV-2 s-protein does not explain the differences in human infectivity between the two SARS-CoV variants.^{6–8,10} However, inhibition of the initial viral adhesion event is still a valid mechanism for potential SARS-CoV-2 therapeutics.

The AngII peptide binds to the ACE2 active site prior to catalysis, and a number of peptide-based ACE2 inhibitors have been reported.^{12,13} While there are no reported crystal structures of AngII bound to ACE2, the crystal structure coordinates of the nonpeptide MLN-4760 (Figure 2) in complex with ACE2 have been published (PDB-ID: 1R4L).¹⁴ When the picomolar inhibitor of the ACE2 active site,¹⁵ MLN-4760 (hereafter referred to as MLN), binds to ACE2, a conformational change to the entire protein is observed by crystallography.¹⁴ Native *apo*-ACE2 is shown in Figure 3A (from PDB-ID: 1R42),¹⁴ adjacent to an equivalent representation of *holo*-ACE2 in Figure 3B (from PDB-ID: 1R4L).¹⁴ It is apparent that there is a large conformational change upon the binding of the small molecule ligand, MLN, which acts to envelope or close around the bound active site ligand via a hinge-bending of two subdomains of the active site domain. There is a 4.4 Å RMSD difference between the protein heavy atoms of *apo*- and *holo*-ACE2 by crystallography¹⁴ (we determined this using ACE2 as the reference for the minimum

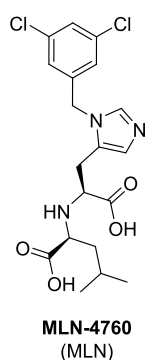


Figure 2. Structure of the small molecule, active site inhibitor of ACE2¹⁵ from PDB-ID: 1R4L¹⁴ or MLN-4760. This molecule is referred to as “MLN” throughout this paper.

least-squares fit). The s-protein binding site, or the ACE2 325-loop and the α -1 and α -2 N-terminal helices of ACE2 (Figure 1), undergoes the most conformational change when MLN binds to *apo*-ACE2, and this change in conformation is as high as 5.5 Å RMSD for these motifs as per the crystal structure (all RMSD values in this paper are calculated by first aligning to the entire ACE2).¹⁴ It is important to determine whether these changes in conformation are capable of altering the binding of s-protein to ACE2.

There is a degree of urgency to develop antiviral therapies for SARS-CoV-2 due to the considerable economic, social, and health impacts that this virus has had worldwide. While there has been some computational work dedicated to helping with this crisis,^{16–20} more detailed studies are required to assist with the development of a therapeutic. Computational methods, especially molecular dynamics based methods, have played an important role in modeling SARS-CoV-2 s-protein dynamics and interactions thus far,²² and there is a scope to use *in silico* tools to help further with the fight against Covid-19. Some modeling work has been reported, where the authors targeted either the s-protein binding site or the s-protein RBD in an

effort to design novel inhibitors of s-protein binding.^{17–20,23–28}

It is becoming increasingly common practice to employ free energy methods to assist drug design,^{29–46} and studies that provide a theoretical basis to guide drug design efforts are useful. However, we contend that the end point approximation and steered methods applied in recent studies to determine the free energy of binding for s-protein to ACE2^{16–20} are potentially challenging to perform accurately for such a large and flexible system. It should be stressed that end point methods do not sample the entire reaction pathway for protein–protein binding/unbinding events. Similarly, it is unlikely that short, nanosecond time scale steered simulations, using a single order parameter to model the reaction pathway, would afford a reliable estimate of the unbinding free energy. It is also likely that the values computed for the s-protein binding free energy in recent studies^{16–20} do not sufficiently account for the entropy changes during the binding/unbinding event. Further, it is well-established that the accuracy of end point methods is often dependent on the specific protein and the value of the dielectric constant used in the calculation of solvation enthalpies.^{47–49} Therefore, the end point methods may not be sufficiently reliable for quantifying the binding enthalpy and entropy of the SARS-CoV-2 s-protein RBD associated with ACE2. This difficulty is also in part due to the current lack of a reliable value of the experimental binding free energy for comparison with those predicted by theoretical free energy calculation methods. This is best illustrated by the fact that the value of K_D for SARS-CoV-2 s-protein binding has been reported to differ by up to 5-fold depending on the experimental method and on the s-protein construct used.^{9,10}

Computational studies where the authors compare SARS-CoV and SARS-CoV-2 s-protein binding free energy values have been reported. For example, Spinello et al.²⁴ used a crystal structure of the SARS-CoV s-protein RBD/ACE2 complex⁵⁰ and a cryo-EM structure of the SARS-CoV-2 s-protein RBD bound to ACE2.⁹ Subsequently, the authors performed 1.0 μ s long molecular dynamics (MD) simulations to investigate the interactions between ACE2 and the two proteins. The

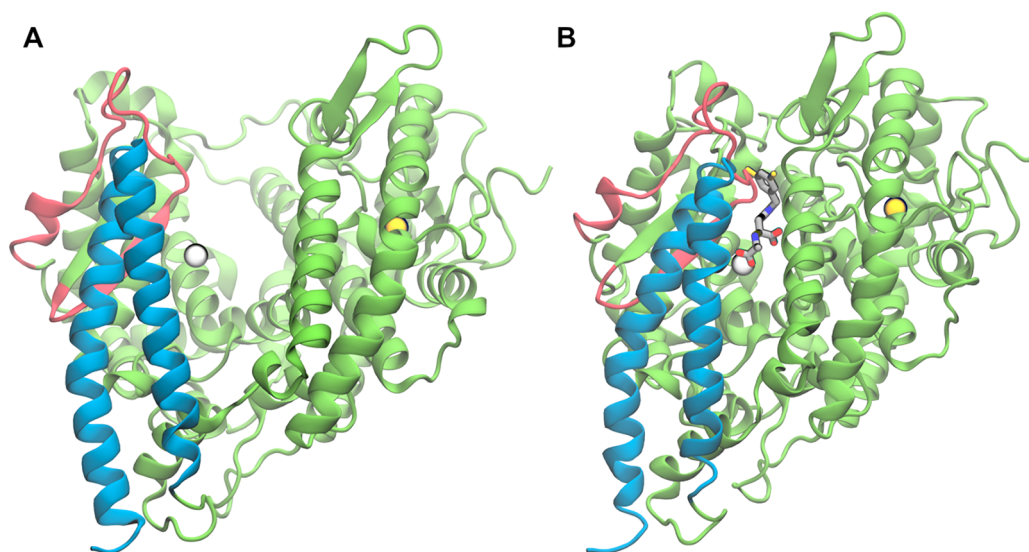


Figure 3. (A) *apo*-ACE2 from PDB-ID: 1R42 represented as light green ribbons. The N-terminal helices are shown as blue ribbons, and the 325-loop is colored red. The SARS-CoV-2 s-protein binds to these motifs. (B) Equivalent representation of *holo*-ACE2 from PDB-ID: 1R4L with MLN bound to the active site. The inhibitor has a stick representation with gray carbon, blue nitrogen, red oxygen, and yellow chloride atoms. Catalytic zinc and chloride ions are shown as silver and yellow spheres.

Molecular Mechanics-Generalized Born Surface Area (MM-GBSA)¹⁶ end point approximation was used to estimate the binding enthalpies of SARS-CoV and SARS-CoV-2 s-proteins with ACE2. It was found that the SARS-CoV-2 s-protein RBD had a higher binding enthalpy than the SARS-CoV s-protein RBD. These findings were replicated by Amin et al.,¹⁷ who reported a similar MD analysis of SARS-CoV and SARS-CoV-2 s-proteins bound to ACE2. These authors demonstrated that the improved binding strength of the SARS-CoV-2 s-protein over the SARS-CoV s-protein was due to multiple mutations in the SARS-CoV-2 s-protein that resulted in stronger interactions with ACE2, as suggested in recent experimental literature.^{11,51} These results are congruent with those reported by Ali and Vijayan²⁰ who ran 1.0 μ s MD simulations of SARS-CoV/SARS-CoV-2 s-protein in complex with ACE2. Ali and Vijayan²⁰ then subjected these trajectories to MM-GBSA analysis and found that the different, stable interactions from the SARS-CoV-2 s-protein to ACE2 resulted in an improved binding free energy with ACE2, relative to the SARS-CoV s-protein. In a detailed study where SARS-CoV/SARS-CoV-2 s-protein binding strength is theoretically compared by an end point method, Ghorbani et al.²³ subject multiple microsecond MD simulations of both s-protein variants bound to ACE2 to Molecular Mechanics-Poisson–Boltzmann Surface Area (MM-PBSA) analysis. They found that the SARS-CoV-2 s-protein bound to ACE2 with a 2.7-fold higher binding enthalpy than the s-protein from the original SARS-CoV. A similar MM-PBSA analysis was performed on trajectories containing ACE2 bound to SARS-CoV-2 s-protein mutants. Ghorbani et al.²³ suggest from their combined results that SARS-CoV-2 s-protein RBD residues Lys-417, Leu-455, Phe-486, Gln-493, Gly-496, Asn-498, Thr-500, Asn-501, Gly-502, and Tyr-505 are each important for binding with ACE2. Targeting these specific residues may be a valid design strategy for anti-SARS-CoV-2 drugs.

Computational studies have also been reported where the authors attempted to inhibit the SARS-CoV-2 s-protein interaction with small molecules and peptide-mimetic inhibitors. Saurabh and Purohit¹⁸ focused on 23 residues from the first N-terminal helix of ACE2. They used MD simulations and free energy calculations and showed that this 23-residue peptide, as well as a mutated variant, bound to the SARS-CoV-2 s-protein RBD with high affinity. Renzi and Ghersi²⁸ utilized similar MD-based methods in an *in silico* study, and they report a putative minimum binding epitope from the ACE2 N-terminal helices. This smaller peptide motif had retained binding strength for the s-protein RBD. These two computational studies where the authors report ACE2 mimetic peptide inhibitors of s-protein binding could form the basis for the design of potential peptide-based SARS-CoV-2 therapeutics. Garcia-Iriepa et al.¹⁹ docked several small molecules into ACE2. They then performed steered MD simulations³⁸ and measured the force required to pull the s-protein RBD from ACE2 in the presence and absence of small molecules bound to the ACE2 s-protein binding site. The authors found that the unbinding free energy from steered MD simulations was higher in the absence of a small molecule bound to the s-protein binding site. The authors Han and Král²¹ also proposed peptide mimetic inhibitors of s-protein recognition based on the N-terminal, α -1 and α -2 helices of ACE2 and combined this scaffold with the Asn-325 loop of ACE2 (Figures 1 and 3). Han and Král²¹ showed that the truncated ACE2 N-terminal helices and a shortened Asn-325 loop motif can be covalently

combined to form a large peptide macrocycle and proposed several peptide mimetic inhibitors of s-protein binding based on this concept. The authors ran a series of MD simulations and showed that their large, peptide macrocycles maintain the secondary structure required for s-protein binding. Using simple electrostatic calculations, Han and Král²¹ showed (qualitatively) that each of their ACE2 mimetic peptides maintained favorable interactions with the SARS-CoV-2 s-protein.

While we focus on the SARS-CoV-2 s-protein RBD in this study, there is evidence that other portions of this s-protein trimer also contribute to the SARS-CoV-2 to ACE2 binding strength. The SARS-CoV-2 s-protein has 22 glycosylation sites that were originally thought to play a role in shielding the virus from the host immune system.⁵² It is now known that these glycosylations of the s-protein may confer additional flexibility at the hinge points of the multidomain s-protein and allow multiple s-protein trimers to interact with the flat host cell surface.⁵³ Importantly, Casalino et al.⁵⁴ ran multiple microsecond MD simulations of the full s-protein and found that the N-glycosylation of s-protein RBD residues N-165 and N-264 played a role in the conformational dynamics of the s-protein. Further evidence that portions of the s-protein distal to the RBD play an important role in s-protein binding was reported by Qiao and Olvera de la Cruz⁵⁵ who performed several 100 ns molecular dynamics simulations. These authors found that the SARS-CoV-2 s-protein binding affinity with ACE2 was reduced by 34% in the absence of the s-protein poly basic cleavage sites. These sites are on the s-protein and are involved in the viral fusion event but are located more than 10 nm away from the s-protein RBD. This combined evidence^{53–55} suggests that, while the inhibition of the interaction between the SARS-CoV-2 s-protein RBD and ACE2 is a valid mechanism for potential anti-SARS-CoV-2 therapeutics, the binding of the SARS-CoV-2 s-protein with ACE2 is still influenced by other portions of the s-protein than the RBD. We aim to determine the effect that a distal active site bound MLN inhibitor of ACE2 (Figure 2) would have on modulating the conformation of the ACE2 N-terminal helices, identified as the s-protein binding site, thus potentially reducing s-protein RBD binding.

There is currently no published work where the authors determine the effect that a bound active site inhibitor, MLN, previously shown to cause conformational changes in ACE2, would have on SARS-CoV-2 s-protein/ACE2 binding strength. Here, we investigate whether the conformational changes induced by the binding of MLN to ACE2 (Figure 3) affect the SARS-CoV-2 s-protein binding energy. In 2005, Li et al.⁵⁶ ran laboratory experiments to determine whether the conformational changes to ACE2 when MLN is bound reduced the original SARS-CoV s-protein binding strength. The authors performed an assay to measure the infectivity of SARS-CoV in the presence and absence of MLN. Li et al.⁵⁶ found that the binding of SARS-CoV s-protein did not affect the enzymatic activity of ACE2. The authors also found that, in the presence of MLN, the infectivity of the original SARS-CoV was unaffected. It is, however, possible that the results of similar experiments applied to novel SARS-CoV-2 may vary due to the multiple mutations between the SARS-CoV/SARS-CoV-2 s-protein RBDs.¹¹ Indeed, while Li et al.⁵⁶ found that the binding of SARS-CoV s-protein did not affect enzymatic activity, more recently, Lu and Sun⁵⁷ showed that SARS-CoV-2 s-protein binding with ACE2 affects the ACE2 catalytic activity. This finding suggests some differences in how SARS-

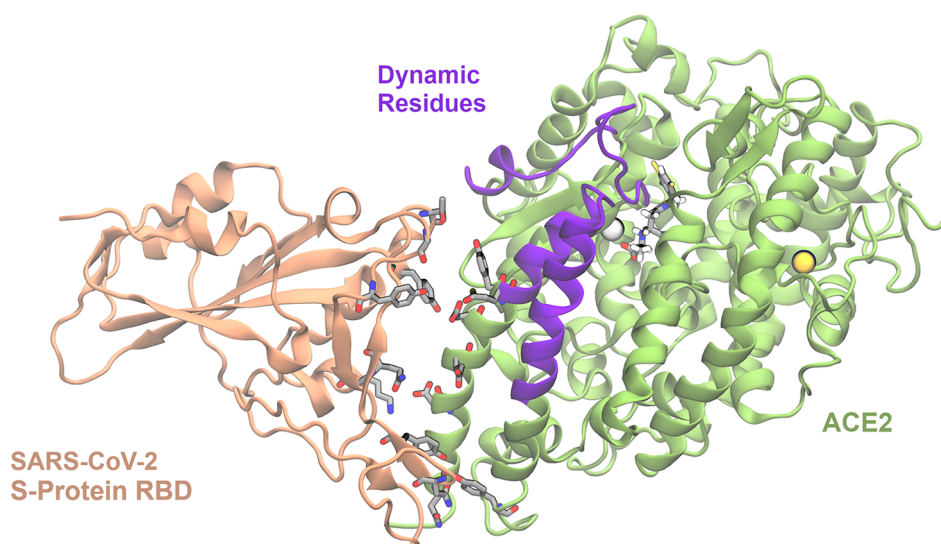


Figure 4. (A) Initial structure of the MLN/ACE2/s-protein complex by combining the coordinates of MLN/ACE2 from PDB-ID: 1R4L and the s-protein RBD from PDB-ID: 6M0J. The ACE2 protein is given a light green ribbon representation, except for the residues that deviate most from the *apo*-ACE2 reference structure (Table 1). These residues are illustrated with purple ribbons. The SARS-CoV-2 s-protein RBD is shown in an orange ribbon representation. Key interacting residues from the ACE2/s-protein complex crystal structure (PDB-ID: 6M0J) are given a stick representation with the hydrogens omitted for clarity. Catalytic zinc and chloride ions are shown as silver and yellow spheres.

CoV/SARS-CoV-2 s-proteins affect ACE2. It is therefore not unreasonable that a bound MLN could also have a different effect on SARS-CoV-2 infectivity compared to the related effect on SARS-CoV. Further, the extent by which the ACE2 to SARS-CoV/SARS-CoV-2 s-protein binding affinity must be reduced to see a loss in infectivity *in vitro* is unclear. It is likely that infectivity would be reduced only once the energetic penalty to ACE2/s-protein binding is sufficiently high, i.e., above a certain threshold yet to be determined. It is therefore possible that Li et al.⁵⁶ did not observe reduced infectivity for SARS-CoV in the presence of MLN *in vitro*, if the conformational penalties imposed to s-protein binding were not high enough. With these considerations, in this study, we aim to determine the extent (if any) of the energetic penalty imposed to ACE2/SARS-CoV-2 s-protein binding, when MLN is bound to ACE2. Based upon the theoretical demonstration of this concept, future work could then focus on designing modulators of ACE2 that enhance the conformational disorder to the ACE2 s-protein binding site and further weaken the SARS-CoV-2 to ACE2 attachment. Such distal modulators that cause conformational lability to the N-terminal helical region of ACE2 could introduce further energetic penalties to s-protein binding with ACE2, facilitating the development of COVID-19 treatments that are potentially independent of future viral s-protein mutations. In this study, we explore the hypothesis that the 5.5 Å RMSD conformational shift in the s-protein binding site of ACE2, when the inhibitor MLN binds to the active site (Figure 3), may perturb the binding of s-protein. To theoretically evaluate the validity of this hypothesis, we employ all-atom MD simulations to investigate the induced ACE2 conformational changes due to the presence of ACE2 active site inhibitor MLN and their thermodynamic (free energy) consequences for s-protein binding. The MD simulations were performed with the following systems:

- System 1: *apo*-ACE2 (PDB-ID: 1R42, Figure 3A)
- System 2: *holo*-ACE2 (PDB-ID: 1R4L, Figure 3B) with bound active site inhibitor MLN (the model named MLN/ACE2 for ease of discussion)

- System 3: *apo*-ACE2 complex with SARS-CoV-2 s-protein RBD (PDB-ID: 6M0J, Figure 1)
- System 4: *holo*-ACE2 (MLN/ACE2) complex with s-protein RBD (the model was generated as described in the Methods)

From analyses of these systems, we aim to gauge the effects that the binding of MLN would have on s-protein binding mode and infer the system entropy change upon the s-protein/ACE2 interaction by monitoring the RMSD changes in ACE2 throughout these four systems. Further, to test for changes in the enthalpic benefit or penalties to s-protein binding, we monitor the interactions observed in PDB-ID: 6M0J for systems 3 and 4. From this information, we anticipate to determine whether s-protein binding strength can be reduced in *holo*-ACE2 with respect to *apo*-ACE2.

METHODS

All molecular models were constructed using the Maestro software suite.⁵⁸

Construction of ACE2 and ACE2 Complex Models.

Crystal structures are reported for native ACE2 as defined in systems 1 to 3 at the end of the Introduction.^{6,14} To generate the ACE2 complex detailed in point (4) (the MLN/ACE2/s-protein complex), we aligned ACE2 from PDB-ID: 1R4L (system 2) to ACE2 from PDB-ID: 6M0J (system 3) using the Protein Structure Alignment tool in Maestro.⁵⁸ Specifically, the atomic coordinates of the entirety of the ACE2 protein subunit were used for alignment. The 6M0J structure contained the coordinates for the SARS-CoV-2 s-protein RBD bound to ACE2, which were combined with the ACE2 structure from 1R4L to generate the initial structure for the MLN/ACE2/s-protein complex model that was then allowed to equilibrate by MD simulations as described below (Figure 4). In the absence of a native crystal structure, we constructed the initial model of the MLN/ACE2/s-protein as a hybrid of PDB-ID: 1R4L for the MLN/ACE2 coordinates and PDB-ID: 6M0J for the coordinates of the s-protein RBD. After the alignment of the ACE2 protein coordinates from system 3 and MLN/ACE2

protein from system 2, we observed a 4.4 Å RMSD conformational difference to ACE2 when MLN is bound and a 5.5 Å RMSD shift to the residues comprising the α -1 and α -2 N-terminal helices. The superposition of ACE2 from system 2 and system 3 is shown in Figure S1, where conformationally changed residues are given a cartoon representation and unchanged motifs are shown as thin ribbons. This information complements the illustrations shown in Figure 3. It is clear from the inspection of Figure 4 that there is no excessive bias in the initial model of the MLN/ACE2/s-protein complex toward the crystal structure of the ACE2/s-protein complex (PDB-ID: 6M0J). It is evident from Figure 4 that the interactions that are present in the native ACE2/s-protein complex (PDB-ID: 6M0J) are mostly absent in the initial model of the MLN/ACE2/s-protein complex constructed from the hybridized crystal structures. The initial model of system 4 was subject to triplicate MD simulations as described below. To ensure that this initial model was not excessively biased toward the PDB-ID: 6M0J crystal structure, we created two additional initial complex structures by rotating s-protein by $\pm 5^\circ$ around the Z-axis. These two systems with different initial s-protein orientations were each run for 500 ns (see below) to provide evidence that the same interactions with the ACE2 receptor were formed in each case. Representations of the two alternate initial s-protein geometries are shown in Figure S2. A table of interaction distances in the initial system 4 model and of those formed during the simulations of system 4 with the two alternate initial s-protein positionings are shown in Table S2. The data demonstrate that the key interactions observed in PDB-ID: 6M0J (system 3) are spontaneously formed after 400 ns of MD equilibration of each system 4 variant.

The Protein Preparation Wizard⁵⁹ tool in Maestro⁵⁸ was used to protonate all structures at pH 7.0 and remove steric clashes. Missing protein loops were modeled with PrimeX.⁵⁹ All acidic or basic residues (including His) were either protonated or deprotonated with *pdb2gmx* using the default options.⁶⁰ For His residues, this meant that the protomer that maximized hydrogen bonding to adjacent residues/waters/ions was selected. The coordinates for the bound Zn and Cl ions in/near the catalytic site were retained from crystallography.

MD Simulation Procedures. MD simulations were performed using GROMACS 2019.^{61,62} Protein atoms and ions were modeled with CHARMM-36 parameters.⁶³ The CHARMM-GUI Web server was used to generate GROMACS topologies for MLN.⁶⁴ Periodic boundary conditions⁶⁵ were set up so that the protein–ligand complex was centered in a periodic cell, where the maximum distance of the solute from the boundary of the cell was 0.8 nm. Software within GROMACS was used to wrap the solute into the triclinic cell, such that the periodic images of this triclinic cell formed an elongated dodecahedron. For these triclinic periodic cells, the approximate cell lengths of systems 1 and 2 were $10 \times 10 \times 7$ and $10 \times 10 \times 6$ nm. For systems 3 and 4, the periodic cell lengths were approximately $13.5 \times 13.5 \times 9.5$ and $13 \times 13 \times 9$ nm. The protein/ligand systems were solvated to a density of approximately 1.0 g mL^{-1} with explicit TIP3P water.⁶⁶ The overall charge of the system was made neutral through the addition of chloride counterions to compensate for the 25^+ charge of the protein with bound Zn/Cl ion cofactors and the 2^- charge of MLN when bound. Additional sodium and chloride ions were added to make a total salt concentration of $\sim 150 \text{ mM}$ to mimic physiological solution conditions. The resultant models (1, 2, 3, and 4) comprised 68 802, 68 080,

166 309, and 150 704 atoms, respectively. Simulations used a 2 fs time step, and neighbor searching was performed every 80 ps for the initial equilibration phases. These settings were changed for production runs, where “heavy hydrogens” were applied to the protein,⁶⁷ allowing for a 5 fs time step and neighbor searching every 200 ps. To validate the application of a 5 fs time step, we performed benchmark simulations with resultant data presented in Table S1. The results demonstrate that the simulations with a 5 fs time step afforded similar results to those with a 2 fs time step (using “normal” hydrogen and heavy atom masses), and so, the larger time step was used to expedite results. The default Verlet integrator was used.⁶⁸ The LINCS algorithm⁶⁹ was used on all nonwater atoms to maintain rigid bond lengths. The default SETTLE algorithm⁷⁰ was used to maintain correct bond lengths for the TIP3P water molecules. Coulombic and Lennard–Jones potential cutoffs of 1.4 nm were used for short-range interactions, and the Particle Mesh Ewald (PME)⁷¹ algorithm was used to account for electrostatic interactions beyond this range.

Each system was set up using the following procedure. The systems were subjected to an unrestrained, steepest descent energy minimization until the maximum force on any atom was less than $500 \text{ kJ mol}^{-1} \text{ nm}^{-1}$. The system was equilibrated using unrestrained simulations: (1) 1 ns NVT using the Berendsen thermostat (310 K), (2) 1 ns NPT using the Berendsen barostat (1 bar) and the V-Rescale thermostat (310 K),⁷² and (3) 10 ns NPT using the Parrinello–Rahman barostat⁷³ (1 bar) and the V-Rescale thermostat (310 K). The third equilibration step was performed for 10 ns to ensure that the system had equilibrated, and the system total energy and the protein heavy atom RMSD were monitored to determine whether this was the case. After the three equilibration phases, the production runs for structural analysis were performed in the NPT ensemble with the Parrinello–Rahman barostat and the V-Rescale thermostat with time constants of $\tau_p = 40 \text{ ps}$ and $\tau_t = 0.1 \text{ ps}$. All production runs were for 500 ns for systems 1 to 3 and $1.0 \mu\text{s}$ for system 4, and for each system 1–4, the simulations were repeated three times from randomized initial velocities generating independent trajectories. For system 4, the first 400 ns of each triplicate $1.0 \mu\text{s}$ was used as an additional equilibration phase. A total of $6.3 \mu\text{s}$ of real time evolution for all the systems was used for the analyses with more than $8.5 \mu\text{s}$ of MD simulation data accumulated, including equilibration phases.

Analysis: RMSD and Binding Interactions. For each system, all frames of the production runs were retained for analysis, except for system 4 comprising the MLN/ACE2/s-protein complex. As described above, this model was constructed as a hybrid of two crystal structures (PDB-IDs: 1R4L and 6M0J) due to the lack of any other experimental data. Prior to the analysis of this system, it was necessary to ensure that the MLN/ACE2/s-protein complex reached equilibrium at 310 K and 1.0 bar. Therefore, as stated above, the first 400 ns of each production run was considered an additional equilibration phase for simulation system 4 (using the 5 fs time step and hydrogen mass repartitioning for this additional equilibration step). The heavy atom RMSD of the protein and protein motifs were used to quantify the conformational dynamics and motion of the free ACE2 and protein–protein complexes. Changes in RMSD between the two free ACE2 (systems 1 and 2) and the two s-protein ACE2 complex systems (systems 3 and 4) were used to infer the change in entropy upon SARS-CoV-2 s-protein RBD binding

Table 1. Heavy Atom RMSD of ACE2 and ACE2 Motifs Involved in Interactions with the s-Protein from Simulations of apo-ACE2 and the ACE2-s-Protein Complexes^a

simulation system	total ACE2	s-protein binding site of ACE2 ^b	key interacting residues from ACE2 ^c	noninteracting residues of ACE2 within the s-protein binding site ^d	ACE2 residues not belonging to the s-protein binding site
(1) apo-ACE2	2.8 ± 0.4	2.9 ± 0.7	2.8 ± 0.4	2.9 ± 0.7	2.9 ± 0.6
(2) MLN/ACE2	4.8 ± 0.4	6.7 ± 0.8	5.0 ± 0.6	7.8 ± 1.0	4.4 ± 0.3
(3) apo-ACE2/s-protein	3.1 ± 0.2	3.1 ± 0.3	2.5 ± 0.4	3.1 ± 0.4	3.1 ± 0.2
(4) MLN/ACE2/s-protein	4.9 ± 0.2	6.9 ± 0.6	4.8 ± 0.4	8.2 ± 0.7	4.4 ± 0.2

^aRMSD measurements are in Å as a mean ± SD from the simulation ensemble. ^bDefined as the α -1 and α -2 helices of ACE2 plus the protein loop starting at Asn-325. Specifically, residues 19 to 83 and residues 325 to 355. See Figure 1. ^cIncludes those previously determined by Lan et al.⁶ or ACE2 residues: Gln-24, Asp-30, Glu-35, Glu-37, Asp-38, Tyr-41, Gln-42, Tyr-83, Lys-353, and Arg-393. ^dACE2 residues 43 to 74 and 325 to 345 make the least contact with the s-protein RBD.

to ACE2. Interaction distances were used to gauge the binding enthalpy of the s-protein to the two free ACE2 systems. These distances were defined as the distance between the centers of the intermolecular bond donor and acceptor heavy atoms. The binding entropies were not directly calculated due to the inherent difficulties achieving “convergence” of these calculations on such large systems, as has been discussed in recent reviews.^{29–46} It should be noted that, for an accurate calculation of the s-protein binding entropy, the full s-protein trimeric construct would need to be simulated (not just the RBD) and the complete receptor bound complex would also include membrane models to anchor the host/viral proteins. Simulations of systems of this size in all-atom details on the time scales required are not feasible at present.

Analysis: Binding Enthalpy by MM-PBSA. The one trajectory method⁷⁴ was used to perform a MM-PBSA calculation on the 500 ns of MD simulation time per replicate for system 3 and 600 ns of simulation time per replicate for system 4. Only protein atoms were retained for analysis to avoid the large fluctuations in potential energy from the use of explicit water. The frames used for the MM-PBSA calculation were spaced at 5 ns intervals. Therefore, 100 frames per replicate were subject to MM-PBSA analysis in system 3, and 120 frames per replicate were analyzed for system 4. The GROMACS package *g_mmpbsa*⁷⁵ was used to calculate the binding enthalpy using a grid spacing of 0.5 Å, an internal solute (protein) dielectric constant of 40, an external solute (saline) dielectric constant of 80, a solvent probe radius of 1.4 Å, and a γ constant of 0.03 kJ mol⁻¹ Å⁻². The internal solute dielectric constant was chosen on the basis of the recommendation and literature review by Li et al.,⁷⁵ who identified that a value between 20 and 40 was appropriate for the surface of a protein.⁷⁶ The value of γ contributes toward the scaling of the solvent accessible surface area in the calculation of the nonpolar interaction energy of the binding enthalpy.⁷⁵

RESULTS AND DISCUSSION

We have analyzed the impact of the conformational change of ACE2 with bound MLN on the structural and energetic properties of the ACE2/s-protein binding interface. Specifically, in MD simulated systems 3 and 4, we analyzed interaction pairs previously suggested by crystallography for system 3. The changes to specific residues positioning on the MLN/ACE2/s-protein binding interface were observed to affect s-protein binding in the MLN/ACE2/s-protein complex. The RMSD values from the MD generated ensemble were

used to quantify the changes to the ACE2 s-protein binding site. The RMSD values of ACE2 and ACE2 motifs in systems 1 and 2, relative to systems 3 and 4, were used to evaluate the extent of the entropic penalty to s-protein binding with ACE2 or MLN/ACE2. The enthalpy of s-protein binding was evaluated by MM-PBSA and by monitoring the experimentally identified interactions between ACE2 and the s-protein RBD. The distinct changes to ACE2 and ACE2 motifs observed in MD simulations were similar to those previously observed by crystallography (Figure 3) of the free ACE2 and the active site inhibitor MLN bound ACE2 systems (Table 1). For simulation systems 1–4, the structure of ACE2 and the s-protein RBD did not deviate more than 2–3 Å RMSD from the respective crystal structures (as expected). Therefore, in each instance where we mention a conformational change to ACE2 or to an ACE2 motif due to the presence/absence of bound active site inhibitor MLN, we are referring to the same conformational changes as observed by the crystallography of apo-ACE2 and inhibitor-bound ACE2 (described in Figure 3). However, MD simulations revealed a greater degree of conformational change than seen by crystallography (Tables 1 and S3) to ACE2 and its s-protein binding site when MLN is bound. It is important to note that the conformational changes to the s-protein binding site reported here are not affected by the 5 fs time step (Table S1). To quantify the changes in geometry to the ACE2 s-protein binding site, we plotted the evolution of the ACE2 backbone angles, φ , ψ , and ω of residues 1 to 82 (Figure S3). The largest conformational change to the average φ or ψ angles of these residues was observed in the Ile-21 ψ angle, which rotates by $-63.1 \pm 5.1^\circ$ (mean \pm 95% CI). The largest conformational changes were to the backbone ω angles of ACE2 residues 1 to 82, where 16 ω angles rotated more than an average of 20° in either direction when MLN is bound to ACE2 (Figure S3 and Table S3). While there is a clear conformational change to the s-protein binding site for MLN/ACE2 relative to apo-ACE2, the ACE2 side-chain torsions of the s-protein binding site are not noticeably changed in the presence of MLN, consistent with the study reported by Li et al.⁵⁶ for SARS-CoV.

Simulations of the MLN bound ACE2 s-protein complex system 4 presented in Figure 4 were analyzed to determine if the key interactions observed by crystallography of the ACE2/s-protein complex (system 3) were spontaneously reformed in system 4. Data presented in Tables 1, 2, and S2 demonstrate that, after 400 ns of the production MD run, the interactions between MLN/ACE2 and the s-protein spontaneously reformed in all three independent simulations of system 4.

Table 2. Hydrogen Bonds and Salt Bridges at the SARS-CoV-2 s-Protein RBD and Human ACE2 Interface by MD and Crystallography⁶ of the ACE2/s-Protein Complex^a

interaction type	subunit 1: ACE2	subunit 2: s-protein RBD	crystallographic interaction length	model system 3 ACE2/s-protein				model system 4 MLN/ACE2/s-protein			
				mean interaction length by MD ^b	bond occupancy (%) ^{b,c}	MD interaction length when bond is present	minimum interaction length ^b	mean interaction length by MD ^d	bond occupancy (%) ^{d,e}	MD interaction length when bond is present	minimum interaction length ^d
H-bonds	Q-24 (OE1)	N-487 (ND2)	2.6	5.4 ± 0.5	3	3.2 ± 0.2	2.7	4.1 ± 1.1	63	3.3 ± 0.9	2.7
	D-30 (OD2)	K-417 (NZ)	3.0	3.8 ± 1.6	66	3.0 ± 1.6	2.5	3.5 ± 1.1	72	2.9 ± 1.2	2.5
	E-35 (OE2)	Q-493 (NE2)	2.8	3.8 ± 0.9	59	3.2 ± 0.9	2.6	4.2 ± 1.2	48	3.2 ± 0.9	2.7
	E-37 (OE2)	Y-505 (OH)	3.2	3.3 ± 1.5	68	2.4 ± 1.5	1.5	4.2 ± 1.8	46	2.7 ± 1.2	1.6
	D-38 (OD2)	Y-449 (OH)	2.7	4.6 ± 2.3	47	2.5 ± 2.3	1.5	4.5 ± 2.5	50	2.4 ± 1.7	1.5
	Y-41 (OH)	T-500 (OG1)	2.6	3.3 ± 0.5	94	3.2 ± 0.5	2.4	3.3 ± 0.7	93	3.1 ± 1.1	2.4
	Y-41 (OH)	N-501 (N)	3.7	4.5 ± 1.3	57	3.5 ± 1.3	2.8	3.8 ± 0.6	69	3.6 ± 0.6	2.6
	Q-42 (NE2)	G-446 (O)	3.3	6.8 ± 1.5	4	3.4 ± 1.5	2.7	7.7 ± 1.7	1	3.5 ± 1.6	3.3
	Q-42 (NE2)	Y-449 (OH)	3.0	4.7 ± 1.7	41	3.2 ± 1.7	1.8	5.3 ± 1.8	34	3.5 ± 1.5	2.5
	Y-83 (OH)	Y-489 (OH)	3.5	4.1 ± 0.4	45	3.7 ± 0.4	3	3.3 ± 2.4	74	1.9 ± 1.3	1.6
	Y-83 (OH)	N-487 (OD1)	2.7	2.8 ± 0.2	99	2.8 ± 0.2	2.5	3.2 ± 0.8	89^e	3.1 ± 0.4	1.7
	K-353 (O)	G-502 (N)	2.8	2.4 ± 0.9	86	2.1 ± 0.9	1.6	2.7 ± 1.1	76	2.1 ± 0.4	1.6
	R-393 (CZ)	Y-505 (OH)	4.8	5.2 ± 1.1	63 ^c	3.9 ± 1.1	3.4	6.0 ± 1.5	42	4.6 ± 1.3	3.6
	D-30 (OD1)	K-417 (NZ)	3.9	3.8 ± 1.6	65	3.0 ± 1.6	2.5	3.5 ± 1.1	72	2.9 ± 1.2	2.5
D-30 (OD2)	K-417 (NZ)	3.0	3.8 ± 1.6	66	3.0 ± 1.6	2.5	3.6 ± 1.2	68	3.0 ± 1.2	2.5	

^aMean and minimum interaction lengths are measured in Ångströms. All errors are ±1.0 SD. ^bValues are based on every frame of the triplicate 500 ns MD trajectories. A total of 1.5 μs of simulation time was used for each measurement. ^cPercentage occupancy was based on an interaction cutoff of 4.0 Å. This is in line with the definition of hydrogen bonds proposed by Jeffrey⁷⁸ and the definition of a protein salt bridge suggested by Kumar and Nussinov.⁷⁹ In the case of the ACE2-Arg-393 guanidinium, the interaction distance cutoff for atoms interacting with the center of the partial charge was set to 5.3 Å or 4.0 Å plus the CZ to N bond length. We therefore allow for the delocalization of electrons in this functional group where the charge is distributed within a 1.3 Å radius from the center of the partial charge (CZ). ^dValues are based on the last 600 ns of the triplicate 1.0 μs MD trajectories. A total of 1.8 μs of simulation time was used for each measurement. An additional 0.2 μs of MD simulation was utilized for Table S2 to total 2.0 μs of utilized simulation time for the interaction distance measurements of system 4 and its variants. ^eBond occupancies reduced by more than 10% when MLN is bound are highlighted in bold.

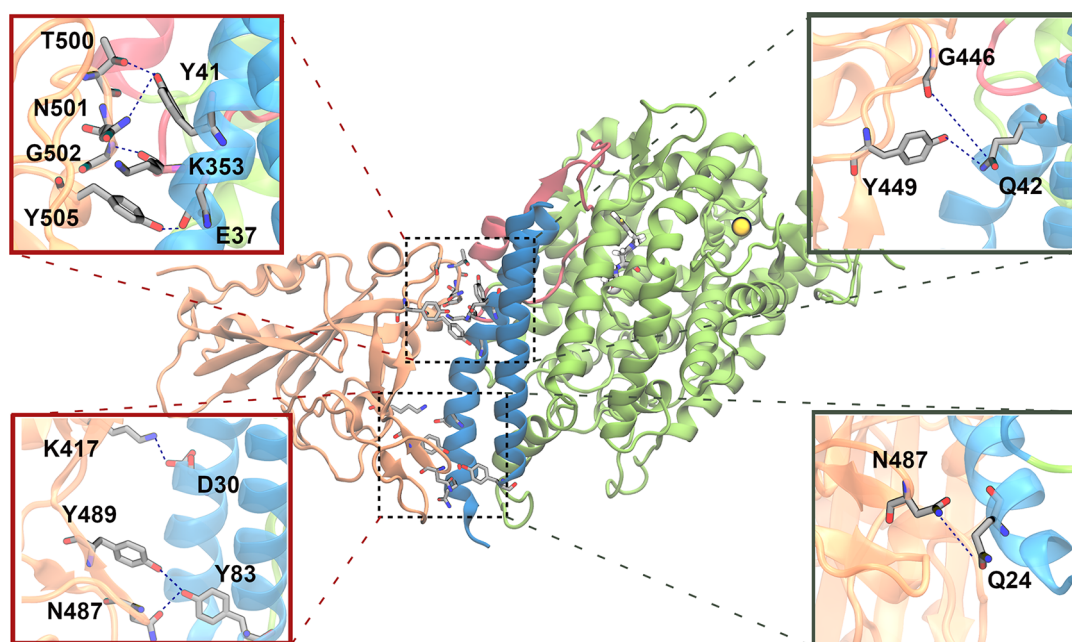


Figure 5. Ribbon representation of an observed typical structure of the MLN/ACE2/s-protein system with key interacting residues shown close up as insets. Coloring of the ribbon representations of the ACE2 motifs is consistent with Figure 3. Less persistent residue pair bond occupancies (<33.3%) across the MD trajectories of either or both ACE2/s-protein and MLN/ACE2/s-protein systems are shown in dark gray boxes (insets on the right). Equivalent graphics where the bond occupancies are >66.7% across the triplicate MD trajectories of ACE2/s-protein or MLN/ACE2/s-protein are shown in red boxes (insets on the left). Specific residue pair interactions are labeled and highlighted with dotted blue lines. Catalytic zinc and chloride ions are shown as silver and yellow spheres.

Moreover, in the two additional simulations with the s-protein initially rotated relative to ACE2 by $\pm 5^\circ$ in the Z-dimension, these same interactions between s-protein and MLN/ACE2 were also spontaneously formed (Table S2). The regions observed to undergo the most significant conformational changes when MLN is bound to ACE2 (system 3) or ACE2/s-protein (system 4) are highlighted in purple in Figure 4. These most conformationally altered residues, when MLN is bound, are not directly involved in the ACE2/s-protein RBD interactions. The RMSD shift attributed to these ACE2 conformational changes (defined in Figure 3) are listed in Table 1. It can be suggested from the observation of Figures 3A,B and 4 and Table S3 and Figure S3 that, due to the tilt inward of the ACE2 N-terminal helices in the presence of MLN, the s-protein RBD may have to hinge onto the ACE2 surface in a different way compared to its binding to apo-ACE2 identified by crystallography.¹⁴ Such a geometric change to the orientation of the s-protein RBD toward the ACE2 binding surface is likely to affect the net binding free energy of s-protein. The changed local geometry of the residues involved in these interactions may also destabilize the interactions, creating an enthalpic penalty to s-protein binding to MLN/ACE2. Detailed analyses and a discussion of the properties is presented below.

Monitoring System Stability. In the reported simulations, the free protein and protein complexes (systems 1–4) were demonstrably stable over the combined 6.3 μ s of simulation time used for the analysis. Specifically, the coordinates of apo-ACE2 and MLN/ACE2 converged to 2.2 ± 0.2 and 2.2 ± 0.3 Å RMSD (mean \pm SD) from the initial structure as averages across the triplicate MD trajectories for each protein. The ACE2/s-protein complex converged to 2.5 ± 0.3 Å RMSD from the initial structure. Ghorbani et al.²³ have reported MD simulations of the same ACE2/s-protein

complex from PDB-ID: 6M0J as our system 3. These authors showed that, when using the AMBER99SB-ILDN force field,⁷⁷ the protein complex RMSD converged to about 1.5 Å RMSD from the initial structure of their production MD run. The simulation of the MLN/ACE2/s-protein complex model (system 4) appears to be close to equilibrium in the last 600 ns of the production runs (determined by monitoring protein RMSD stability). Throughout the simulation time, an average RMSD of 2.8 ± 0.6 Å was obtained, relative to the initial coordinates of the equilibrated MLN/ACE2/s-protein complex. Interestingly, the RMSD of the inhibitor molecule MLN bound to the ACE2 active site also remained stable with 1.4 ± 0.2 Å RMSD from the initial pose over the 3.3 μ s of combined simulation time analyzed for systems 2 and 4. There was a small increase in the RMSD of MLN (to 2.1 ± 0.3 Å) in the MLN/ACE2/s-protein complex in one of the three independently simulated trajectories due to a rotation in the *m,m*-dichlorophenyl group, which still did not cause the inhibitor dissociation from the active site.

Quantifying Conformational Changes to the ACE2 s-Protein Binding Site. The MD structures of all modeled ACE2 systems were analyzed relative to the native conformation of apo-ACE2 to understand how the binding of s-protein could be perturbed when inhibitor MLN is bound to ACE2. Ensemble RMSD values were obtained relative to an equilibrated apo-ACE2 structure for ACE2 in the systems comprising apo-ACE2, MLN/ACE2, ACE2/s-protein RBD, and MLN/ACE2/s-protein RBD (systems 1, 2, 3, and 4). For the protein heavy atoms, RMSD measurements were calculated relative to an aqueous MD structure equilibrated at 310 K and 1 bar, while the RMSD of inhibitor MLN was measured relative to an equivalent equilibrated crystal pose.¹⁴ The RMSD of apo-ACE2 converged to 2.8 ± 0.4 Å (mean \pm SD) from the equilibrated apo-ACE2 reference structure using an

apo-ACE2 structure subsequent to the 10 ns NPT equilibration phase (Table 1). For the MLN/ACE2 complex, the protein RMSD converged to 4.8 ± 0.4 Å from the same *apo*-ACE2 reference structure. The analysis of the RMSD for the ACE2 residues directly or indirectly involved in the binding interface with s-protein reveals how the dynamics of the ACE2 s-protein binding site were affected by the binding of inhibitor MLN to the ACE2 active site. Any changes to the conformation and dynamics of the s-protein binding site when MLN is bound may affect the strength of the s-protein interaction.

The simulation shows that, when active site inhibitor MLN is bound, the s-protein binding site of ACE2 is significantly more conformationally flexible than the rest of ACE2 (Table 1). In the simulation of *apo*-ACE2, the s-protein binding site converged to 2.9 ± 0.7 Å RMSD from the equilibrated structure, while the rest of the protein converged to 2.8 ± 0.4 Å RMSD relative to the same reference structure. With inhibitor MLN bound to the ACE2 active site, the RMSD of the s-protein binding site increased substantially (Table 1). Specifically, there is an increase of 3.8 Å in the RMSD of the entire s-protein binding site of ACE2, an increase of 2.2 Å in the RMSD of key interacting residues, and an increase in the RMSD of noninteracting residues providing scaffolding to the s-protein binding site of 3.9 Å once the active site inhibitor is bound (Table 1). These increases in RMSD indicate that the ACE2 s-protein binding site is conformationally altered when a ligand binds to the active site. Further, the RMSD of the s-protein binding site was consistently higher than the RMSD change in the rest of the ACE2 protein (Table 1, second, third, and last column). This suggests that the changes in conformation to the s-protein binding site cannot be explained by the large conformational changes to the entire protein observed experimentally and illustrated in Figure 3 showing the *apo*-protein (PDB-ID: 1R42) and the *holo*-protein (PDB-ID: 1R4L).

The large conformational change in the s-protein binding site when inhibitor MLN is bound to ACE2, observed by both MD and crystallography, may not be conducive to the binding of s-protein. The analysis of MD trajectories identified the conformational shift to the s-protein binding site of MLN/ACE2 to be 6.7 ± 0.8 Å RMSD from the same motifs in the *apo*-ACE2 reference structure, which is greater than the conformational change in these motifs observed by crystallography of the same ACE2 structures (5.5 Å RMSD). Moreover, for the most conformationally altered residues in ACE2 identified by MD (residues 43 to 74 and 325 to 345) when inhibitor MLN is bound, the conformational change in these motifs is as high as 7.8 Å RMSD from the equilibrated *apo*-structure (Table 1). We should note that no previous study has identified the ACE2 motif comprising residues 43 to 74 and 325 to 345 to be the most conformationally changed when MLN is bound to ACE2. While the most conformationally altered residues make no direct contact with s-protein (Figure 5), it is possible that the ACE2/s-protein binding pathway will be affected by virtue of the fact that these residues make up a different local environment for the directly interacting residues, relative to *apo*-ACE2. These findings imply that the degree of movement in the ACE2 motifs comprising the s-protein binding site is large, potentially significant, and could have an impact on the mechanism and kinetics of s-protein binding. Specifically, it can be suggested that these conformational changes are likely to alter the kinetics of s-protein binding, as

the s-protein would have to “hinge” onto ACE2 in a different way when active site inhibitor MLN is bound to ACE2.

In the discussion of the entropic component to the s-protein binding reaction with ACE2, we should also consider that the entropic contributions to the binding from the s-protein might be different for s-protein binding to ACE2 in system 2 instead of system 1. The SARS-CoV-2 s-protein is heavily glycosylated, and it is important to discuss the potential effects that this may have on the results found in this study. The multimeric SARS-CoV-2 s-protein has 22 glycosylation sites that are believed to play a role in shielding the virus from the host immune system.⁵² There is also indirect evidence that the glycosylation of the s-protein may confer additional flexibility at the hinge points of the multidomain s-protein²⁰ and allow multiple s-protein trimers to interact with the flat host cell surface.⁵³ Importantly, Casalino et al.⁵⁴ ran multiple microsecond MD simulations of the full s-protein and found that the correct N-glycosylation of s-protein RBD residues N-165 and N-264 played a role in the conformational dynamics of the s-protein RBD. These authors also showed that N165A and N264A variants of the s-protein RBD had reduced binding affinity for ACE2, using biolayer interferometry experiments. We would not expect to see this degree of protein conformational change on the time scales accessed by our MD simulation experiments. Therefore, the absence of residues 1–332 of the s-protein RBD in our models (from PDB-ID: 6M0J) should not affect the results presented here. It is also worth mentioning that Qiao and Olvera de la Cruz⁵⁵ found that the presence or absence of the s-protein poly basic cleavage sites in their models resulted in a difference in s-protein binding strength of up to 34%. Importantly, from our methods, we cannot rule out the possibility that the entropic contributions to s-protein binding may vary depending on what s-protein construct is used and on whether the s-protein is binding to *apo*-ACE2 versus MLN/ACE2. The s-protein RBD used in our modeling may be insufficient in estimating the entropic contributions to binding of the full virus-bound s-protein trimer to membrane-bound ACE2. Therefore, we do not quantify the s-protein conformational change differences between systems 3 and 4 here.

ACE2 Active Site Inhibitor Induces Conformational Changes and Thermodynamic Penalties to s-Protein Binding. We analyzed the effects of MLN inhibitor binding to the ACE2 active site on the structure, dynamics, and energetics of the ACE2 binding interface with s-protein RBD. The data presented below include the RMSD and specific interaction analysis for key residues as identified previously by crystallography as well as several other interactions identified herein by the MD simulations, followed by a theoretical evaluation of the effect of MLN inhibitor on the ACE2/s-protein binding enthalpy.

The shift in RMSD for ACE2 residues 43 to 74 and 325 to 345 (Table 1 and Figure 4) dominates the change in RMSD of the entire ACE2 s-protein binding site when MLN is bound. There was no significant difference observed in the protein conformations upon s-protein binding to MLN/ACE2 compared to the free MLN/ACE2, as indicated by similar RMSD values obtained by MD for these systems (Table 1). This suggests a minimal entropic penalty to the binding of s-protein to ACE2 in the presence of MLN due to the local conformational transitions around the s-protein binding site. As stated, this does not rule out the possibility of different s-protein conformations and kinetics when binding to *apo*-ACE2 versus MLN/ACE2. Variations in the s-protein binding

kinetics or s-protein binding entropies are likely considering the changed geometry and increased mobility of the ACE2 s-protein binding site in MLN/ACE2. This rationale opens up possibilities for an alternative ACE2 active site inhibitor design that would cause more significant conformational lability to the N-terminal ACE2 region (i.e., the s-protein binding region). Such an increase in the ACE2 receptor lability would introduce energetic penalties to the s-protein binding to ACE2. However, if we consider the enthalpic component to s-protein binding alone, we can suggest that the active site inhibitor MLN could perturb the binding of s-protein to ACE2 by reduction of the enthalpic benefit of the s-protein bound ACE2 form. To understand whether the enthalpic contribution to s-protein binding was affected in the presence of an active site inhibitor, the interactions observed by crystallography of the ACE2/s-protein complex were monitored across the MD trajectories for each complex system (Table 2).

Data in Table 2 indicate that the key ACE2/s-protein residue interaction pairs observed by crystallography⁶ maintain generally stable interaction lengths across all MD trajectories (Table 2). There is a 1.4 Å RMSD in the mean interaction lengths between the known residue pairs of system 3 and the corresponding crystal structure, which can be largely attributed to the effects of thermal fluctuations evidenced in MD simulations, not directly observable in the crystallographic structures. There was no appreciable difference between the interactions seen in the simulations of *apo*-ACE2 and MLN/ACE2 in complex with the s-protein RBD. Specifically, the pair interaction lengths of the MLN/ACE2/s-protein complex deviated from those equivalent lengths seen in the simulation of the ACE2/s-protein complex by 0.6 Å RMSD across the entire ensemble. Additionally, the minimum interaction lengths throughout the combined trajectories of ACE2/s-protein and MLN/ACE2/s-protein complexes were different by only 0.5 Å RMSD. These findings indicate that all interactions present throughout the course of the simulations of the ACE2/s-protein complex were generally present, with similar stability, during the simulations of the MLN/ACE2/s-protein complex. In agreement with our findings, Ghorbani et al.²³ reported multiple microsecond MD simulations of SARS-CoV/SARS-CoV-2 s-protein in complex with ACE2 using a different force field (AMBER99SB-ILDN⁷⁷). The authors report similar bond occupancies for the SARS-CoV/SARS-CoV-2 s-protein and ACE2 interaction pairs to the data presented in Table 2 for the SARS-CoV-2 s-protein. The marginal differences can be attributed to variations in sampling times, force field, and the MD parameters employed.

However, while the key interactions between ACE2 and the s-protein RBD were generally maintained in the MD simulations, several other interactions reported from crystallography⁶ were observed to break and reform in both the ACE2/s-protein and MLN/ACE2/s-protein complexes (Table 2). Generally, upon the binding of MLN to ACE2, there was an increase in the bond occupancy of 60% for the ACE2-Gln-24 interaction and a net cumulative decrease in bond occupancy of 27% for all other interactions presented in Table 2. These decreases in noncovalent bond occupancy are likely to result from the changed local geometry of the ACE2 s-protein binding site (Table 1 and Figure S3 and Table S3). It can be suggested that such changes in bond occupancy could affect the s-protein binding. Specifically, in the simulations of the ACE2/s-protein system (system 3), the ACE2 residues Gln-24 and Asn-487 involved in the interactions with s-protein

had the lowest bond occupancy (Table 2). For this system, the interactions with the s-protein RBD were absent for over 97% of the simulation time. In the simulation of the MLN/ACE2/s-protein complex (system 4), however, the bond occupancy for the ACE2-Gln-24 interaction was 63%, and this is a key difference between the two systems. Further, the ACE2 interaction involving Glu-35 has a bond occupancy of about 59% and 48% with s-protein residue Gln-493 for both systems. This specific interaction pair does not have an equivalent observed by crystallography of the SARS-CoV s-protein RBD in complex with ACE2 and is an interaction unique to SARS-CoV-2 adhesion.⁶ The same is also true for the salt bridge between Asp-30 of ACE2 and Lys-417 of the SARS-CoV-2 s-protein RBD, as this specific interaction also does not have an equivalent in the SARS-CoV s-protein RBD.⁶ We observed this salt bridge starting from ACE2-Asp-30 to exist for 65% to 72% of the time throughout the simulations of both s-protein bound systems (Table 2). While the charge-assisted hydrogen bonding interactions involving ACE2-Asp-30 and Glu-35 have no equivalent in the case of SARS-CoV s-protein binding to ACE2, we found that the interactions were likely moderate in strength when present,⁷⁸ and we did not observe these interactions to be more stable when SARS-CoV-2 s-protein is bound to ACE2. The simulations showed that the most stable hydrogen bond interactions with s-protein were formed by ACE2-Tyr-41 (OH), ACE2-Tyr-83 (OH), and the ACE2-Lys-353 backbone oxygen, none of which have equivalent interaction partners for the binding of SARS-CoV s-protein⁶ (Table 2). Therefore, targeting the ACE2-Tyr-41, Tyr-83, and Lys-353 interactions in the rational design of molecular inhibitors of SARS-CoV-2 s-protein binding can be a possible approach to modulate the ACE2-SARS-CoV-2 interaction. The key interactions presented in Table 2 are graphically shown in Figure 5. Figure 5 (insets, right) shows all residue pairs with the interactions present for less than 33.3% of the combined simulation time for at least one of the two systems (3 or 4). These interactions are potentially less significant for s-protein binding, based on the data in Table 2. Similarly, Figure 5 (insets, left) also shows the *apo*-ACE2 and MLN/ACE2 to s-protein interactions, which were present for more than 66.7% of the simulation time. These persistent interactions are potentially more significant for SARS-CoV-2 s-protein binding and can be suggested for targeting in the design of anti-SARS-CoV-2 therapeutics.

In a study reported by Starr et al.,⁸⁰ the authors performed deep mutational scanning of the SARS-CoV-2 s-protein RBD to determine the effect each mutation would have on s-protein binding affinity with ACE2. It was found that s-protein RBD residues Asn-487, Tyr-489, and Gly-502 were the most mutationally constrained residues, where changes in these specific residues would have a deleterious effect on ACE2 binding. We found that same s-protein RBD residues Asn-487, Tyr-489, and Gly-502 maintained stable interactions with ACE2 partner residues throughout the course of the system 3 simulations (Figure 5 and Table 2), which is congruent with the results reported by Starr et al.⁸⁰ For the interactions involving s-protein residues Asn-487 and Gly-502, an ~10% decrease in bond occupancy upon the binding of MLN to ACE2 was observed in the MD simulations (Table 2). This suggests that the binding of MLN may reduce the interactions between ACE2 and s-protein due to the observed decreased contacts involving these two mutationally constrained residues. Interestingly, the interaction between Gln-42 of ACE2 and

Gly-446 of the s-protein was mostly absent throughout the simulations for both systems (Figure 5 (insets, right) and Table 2). It has been suggested that SARS-CoV-2 Gly-446 contributes to s-protein binding strength by conferring added flexibility to the s-protein RBD, which may reduce the steric hindrance to other key s-protein RBD interactions and/or assist the membrane fusion event, postviral adhesion.^{10,24} Further, Starr et al.⁸⁰ reported that the mutation of SARS-CoV-2 s-protein RBD Gly-446 to most other possible residues has a minimal effect on the binding affinity of the RBD with ACE2, which provides an additional rationale to the hypothesis that this residue assists with the viral fusion event rather than contributes to s-protein adhesion to ACE2, in line with our simulation results.

To obtain a more quantitative measure of the binding enthalpy of the SARS-CoV-2 s-protein to ACE2, MM-PBSA calculations were performed. Specifically, the MM-PBSA method was used to analyze the MD trajectories of ACE2/s-protein and MLN/ACE2/s-protein complexes and compare the binding enthalpies of the s-protein RBD associated with apo-ACE2 vs MLN/ACE2. The results of MM-PBSA analysis are shown in Table S4 for each replicate trajectory. Equations 1 to 3 describe how the dissociation constant, K_D , quantifying the s-protein binding strength is related to the free energy of binding. The Gibbs free energy change to the system caused by s-protein binding to ACE2 is defined as ΔG_{bind} or the free energy of binding; ΔH_{bind} is the binding enthalpy change, and ΔS_{bind} is the change in entropy to the system as s-protein binds to ACE2 with R being the gas constant and T being the system temperature in Kelvin. Importantly, the MM-PBSA method is used to determine ΔH_{bind} as the sum of the changes in van der Waals energy (ΔH_{vdW}), the change in the energy from Coulombic interactions (ΔH_{elec}), the change in solvation enthalpy (ΔH_{solv}), and the change in the nonpolar interaction energy by virtue of the change in the protein–solvent accessible surface area as s-protein binds (SASA_{en}). Due to inherent difficulties with the convergence of entropy calculations with such large systems, we did not compute ΔS_{bind} and ranked the binding energy of s-protein in terms of ΔH_{bind} alone. In this way, it is assumed that the entropic component to the s-protein binding free energy is roughly equal in the two instances. It must be noted that the use of end point methods to rank the interaction strength of protein–ligand complexes is fairly standard,^{49,81} and it is common to rank protein–protein interaction strength using the binding enthalpy alone.⁸²

$$\Delta G_{\text{bind}} = RT \ln(K_D) \quad (1)$$

$$\Delta G_{\text{bind}} = \Delta H_{\text{bind}} - T\Delta S_{\text{bind}} \quad (2)$$

$$\Delta H_{\text{bind}} = \Delta H_{\text{vdW}} + \Delta H_{\text{elec}} + \Delta H_{\text{solv}} + \text{SASA}_{\text{en}} \quad (3)$$

The MM-PBSA analysis of the MLN/ACE2/s-protein complex simulations afforded a ΔH_{bind} value that was more positive than that of the ACE2/s-protein complex, indicating a proportionally higher K_D . We observe a 1.24-fold reduction in the ΔH_{bind} value when MLN is bound to ACE2 as an average of three replicate trajectories (Tables 3 and S4). This reduction in ΔH_{bind} was statistically significant from a one-tailed t test of the two heteroscedastic samples ($p = 0.028$, $\alpha = 0.05$), and there was no overlap in the 95% CI values of ΔH_{bind} for systems 3 and 4 (Table 3). While the average reduction in ΔH_{bind} was seen to be 1.24-fold in the presence of MLN, we

Table 3. Results from the MM-PBSA Analysis of Systems 3 and 4^a

	ACE2/s-protein system 3	MLN/ACE2/s-protein system 4
ΔH_{vdW}	-332 ± 8	-286 ± 37
ΔH_{elec}	-68 ± 2	-62 ± 8
ΔH_{solv}	250 ± 7	223 ± 46
SASA_{en}	-42 ± 1	-35 ± 6
ΔH_{bind}	-194 ± 6	-156 ± 18
95% CI	$-187 > \Delta H_{\text{bind}} > -201$	$-136 > \Delta H_{\text{bind}} > -176$

^aAll variables are defined in eq 3, and data are shown in units of kJ mol^{-1} . All values are a mean \pm SD of three replicate simulations with randomized initial velocities. A 95% CI in ΔH_{bind} is included (also from the three replicate simulations). Raw data is in Table S4.

can conclude from the 95% CI in ΔH_{bind} values that this reduction in ΔH_{bind} could range from 1.06- to 1.48-fold (Table 3) and that the observed reduction in ACE2/s-protein binding is likely moderate in effect. It is important to note that all energy values reported in Table 3 should only qualitatively correlate with the experiment due to the simplicity of the implicit solvation model. However, while the true values of ΔH_{bind} could be expected to be some factor higher or lower than those reported here, we predict that a reduction in s-protein binding strength when the active site inhibitor is bound to ACE2 should be observed by the experiment. Further, from this data, we cannot infer a reduction in SARS-CoV-2 infectivity, as was investigated in experiments by Li et al.⁵⁶ for the original SARS-CoV, although we can suggest that SARS-CoV-2 s-protein binding strength is likely reduced when MLN is present in the system. Closer inspection of the interactions in each trajectory revealed that, while similar stability in the interaction pairs is observed throughout the ensemble simulations of the ACE2/s-protein complex (Table 2), for the MLN/ACE2/s-protein complex, there was a noticeable decrease in noncovalent bond occupancy for the following ACE2 residues: Glu-35, Glu-37, Tyr-83, Lys-353, and Arg-393 (Table 2 and Figure 6). In fact, across the three independent simulations of system 4, there was a decrease in bond occupancy for these residues of more than 10% (Figure 6). The destabilization of these interactions appears to affect the value of ΔH_{bind} (Table 3), and we suggest that these interactions are more likely to break due to the changed geometry of the s-protein binding site in MLN/ACE2 (Figure 3 and Tables 1 and S3).

It has become common to report a per-residue decomposition of the binding enthalpies from free energy analysis of the binding pathway end points and posit key interacting residues in the SARS-CoV-2 s-protein RBD that improve binding strength. Spinello et al.²⁴ performed 1.0 μs long MD simulations to investigate the interactions between the two s-protein RBD variants and ACE2. The Molecular Mechanics-Generalized Born Surface Area (MM-GBSA)¹⁶ end point approximation was used to estimate the binding enthalpies of SARS-CoV and SARS-CoV-2 s-proteins with ACE2. They found that the s-protein RBD from SARS-CoV-2 had a higher affinity for ACE2 than the equivalent SARS-CoV s-protein RBD, which was in qualitative agreement with the experiment.^{9,10} The authors also found that the enthalpic contributions of ACE2 residues Gln-24, Tyr-41, Tyr-83, and Lys-353 were negative, inferring that these residues contributed to increased binding strength. However, Spinello et al.²⁴ found that Asp-38 of ACE2 was not conducive to s-

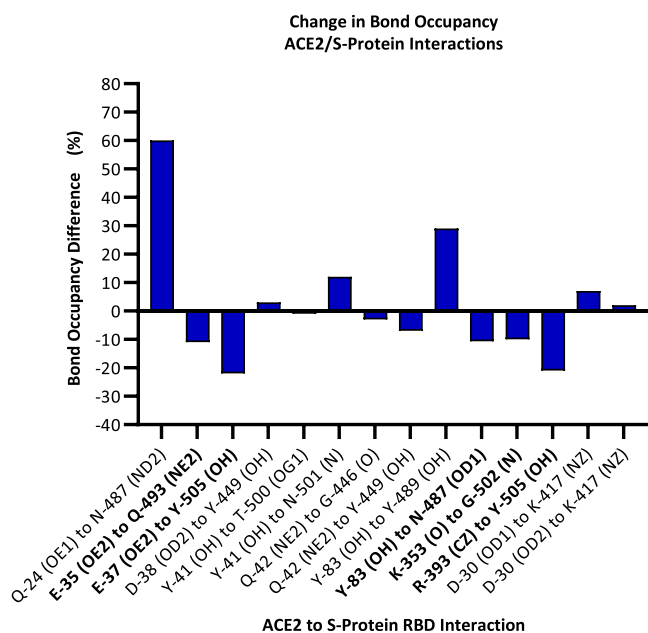


Figure 6. Difference in bond occupancy for key ACE2/s-protein interactions when MLN is bound to ACE2. Interactions that are destabilized by more than 10% are labeled in bold. Raw data is in Table 2.

protein binding, contributing to an enthalpic penalty to binding. The results of our study are consistent with those reported by Spinello et al.²⁴ in that we see stable ACE2 to s-protein interactions in each of these residues (highlighted in Table 2). Further, if the ACE2-Asp-38 interaction with the SARS-CoV-2 s-protein RBD contributes an enthalpic penalty to the binding of s-protein, our simulations showed that this penalty would be unaffected when MLN is bound to ACE2 (Table 3 and Figure 6). We, however, demonstrated that ACE2-Tyr-83 and ACE2-Lys-353 interactions are destabilized by more than 10% when MLN is bound to ACE2 (Figure 6), which suggests that the enthalpic benefit of these interactions reported by Spinello et al.²⁴ would be perturbed when MLN is bound to ACE2. At the same time, another interaction between ACE2-Tyr-83 (to s-protein-Tyr-489) is stabilized in the presence of MLN. This stabilization of the ACE2-Tyr-83 to s-protein-Tyr-489 interaction could potentially counteract the effect of the destabilization of the ACE2-Tyr-83 to s-protein-Asn-487 interaction on ΔH_{bind} . Interestingly, Spinello et al.²⁴ found that the ACE2-Gln-24 to s-protein-Asn-487 interaction was thermodynamically favored for s-protein binding. Our results here suggest that the bond occupancy of this interaction is improved by 60% when MLN is bound to ACE2. Perhaps the moderate, 1.24-fold reduction of ΔH_{bind} that we observe for s-protein binding could be higher if the ACE2-Gln-24 interaction was not stabilized in MLN/ACE2/s-protein (system 4) relative to system 3, suggesting that Gln-24 as a potential target for inhibiting the s-protein adhesion.

The results of Spinello et al.²⁴ are consistent with results reported by Amin et al.,¹⁷ who describe a similar free energy analysis of SARS-CoV and SARS-CoV-2 s-proteins bound to ACE2. Amin et al.¹⁷ aimed to demonstrate that the improved binding strength of the SARS-CoV-2 s-protein over the SARS-CoV s-protein was due to multiple mutations in the SARS-CoV-2 s-protein, resulting in improved interactions with ACE2. These authors also used an end point approximation

method to quantify the per-residue binding free energy contributions of the SARS-CoV-2 s-protein RBD and found that the improved binding free energy of the SARS-CoV-2 s-protein RBD was largely due to the strength of the Lys-417 interaction from the SARS-CoV-2 s-protein RBD with Asp-30 of ACE2. The ACE2-Asp-30 to SARS-CoV-2 s-protein-Lys-417 interactions were also persistent in our simulations of the ACE2/s-protein and MLN/ACE2/s-protein complexes (Table 2, Figures 5 and 6), albeit this charge–charge interaction was not the most stable of all the crystallographic interactions that we monitored.

Ali and Vijayan²⁰ performed 1.0 μs MD simulations of the SARS-CoV/SARS-CoV-2 s-protein in complex with ACE2 and found stable interactions between ACE2 and the SARS-CoV-2 s-protein. It was reported that the ACE2-Asp-30, ACE2-Glu-35, ACE2-Asp-38, and ACE2-Lys-353 interactions with the SARS-CoV-2 s-protein were stable on the microsecond time scale. The MM-GBSA analysis showed that the stable interactions between SARS-CoV-2 s-protein and ACE2 resulted in a moderately improved binding energy with ACE2, relative to the SARS-CoV s-protein. These results from Ali and Vijayan²⁰ are congruent with the results reported here (Table 2) in that we also see stable interactions between ACE2 and the s-protein complex for ACE2 residues Asp-30, Glu-35, Asp-38, and Lys-353. Interestingly, we found that bound MLN destabilizes two key interactions that Ali and Vijayan²⁰ posited were important for s-protein binding. Specifically, we observed here that the ACE2-Glu-35 to s-protein-Gln-493 and ACE2-Lys-353 to s-protein-Tyr-505 interactions are destabilized by more than 10% (Figure 6). It can be suggested that the destabilization of these interaction pairs contributed to the decreased s-protein binding enthalpy ΔH_{bind} to the MLN/ACE2 receptor. Further, we find that the ACE2-Asp-38 interaction with SARS-CoV-2 s-protein is not substantially changed when MLN is bound to ACE2 (Figure 6), inferring a minimal effect on ΔH_{bind} for this residue interaction pair (Table 3).

Ghorbani et al.²³ reported multiple microsecond MD simulations of SARS-CoV and SARS-CoV-2 s-protein RBD (and several s-protein mutants) in complex with ACE2 using the AMBER force field.⁷⁷ The authors also performed MM-PBSA analysis on the last 400 ns of the trajectory of wild-type SARS-CoV and SARS-CoV-2 s-protein in complex with ACE2 to quantify s-protein RBD binding strength in each case. Their MM-PBSA analysis showed that the s-protein binding enthalpy was improved by more than 2.7-fold by for SARS-CoV-2 s-protein, which is in qualitative agreement with previous experimental and theoretical results discussed in this paper. It was found that SARS-CoV-2 s-protein RBD residues Lys-417, Phe-486, Gln-493, Gly-496, Asn-498, Thr-500, Asn-501, and Tyr-505 contributed to the MM-PBSA binding energy with ACE2 at -15 kJ mol^{-1} per residue. All other interfacial residues of the SARS-CoV-2 s-protein either were not as enthalpically beneficial to ACE2 adhesion or contributed to an enthalpic penalty, as predicted by MM-PBSA. The s-protein-Lys-417 salt bridge with ACE2-Asp-30 had an enthalpic benefit of at least -50 kJ mol^{-1} in this study, which is in agreement with the results by Amin et al.¹⁷ discussed above. It was also found that the following SARS-CoV-2 s-protein RBD mutations penalized the MM-PBSA binding enthalpy with ACE2 by more than 40 kJ mol^{-1} : K417A, L455A, T500A, N501A, and G502A. It should be restated that MM-PBSA binding enthalpy values should correlate with experimental

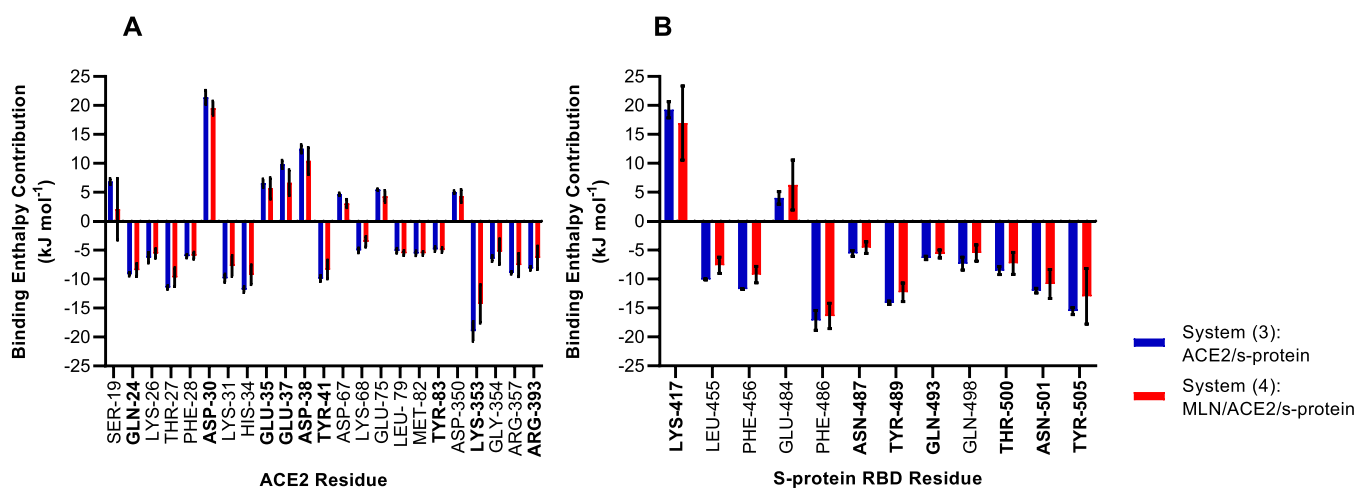


Figure 7. Per-residue energy decomposition (kJ mol^{-1}) from MM-PBSA for (A) ACE2 residues and (B) SARS-CoV-2 s-protein RBD residues involved in the ACE2/s-protein interaction. Only residues involved in an enthalpic benefit or penalty greater than 5 kJ mol^{-1} in system 3 are shown. Residues involved in the key interactions identified from crystallography (PDB-ID: 6MOJ) and listed in Table 2 are represented in bold. Error bars represent a 95% CI from three replicate MM-PBSA calculations, using randomized initial velocities for each trajectory.

trends in protein adhesion strength. Interestingly, each of the mutations studied by Ghorbani et al.²³ had a similar effect on the MM-PBSA binding enthalpy as we observed herein when MLN is bound to ACE2 (Table 3). Ghorbani et al.²³ suggested that SARS-CoV-2 s-protein RBD residues Lys-417, Leu-455, Phe-486, Gln-493, Gly-496, Asn-498, Thr-500, Asn-501, Gly-502, and Tyr-505 are important for adhesion with ACE2 and targeting these residues could be a valid strategy for the design of therapeutics. Interestingly, when MLN is bound to ACE2, we found a greater than 10% reduction in bond occupancy for the following s-protein residues that were reported to be important by Ghorbani et al.:²³ Gln-493, Gly-502, and Tyr-505 (Figure 6). The destabilization of the key interactions these residues are involved in confirms the effect of MLN on disrupting s-protein binding. Future ACE2 active site inhibitors could therefore be designed to optimize the conformational disruption to the s-protein binding site and further reduce s-protein binding.

To assist with potential drug design efforts targeting the ACE2/SARS-CoV-2 s-protein interactions, we report here per-residue binding energy contributions for all residues where the enthalpic penalty or benefit to binding was greater than 5 kJ mol^{-1} (Figure 7). Specifically, enthalpic contributions between -5 and 5 kJ mol^{-1} in system 3 are not shown in Figure 7, but all raw data is included in Table S5. We include per-residue binding energy values here to complement previous computational studies, where authors also report the per-residue enthalpic contributions to binding.^{20,23,24} We anticipate this information regarding which ACE2 and SARS-CoV-2 s-protein residues are enthalpically favored in the interaction could assist with the discovery of inhibitors of ACE2/s-protein complex formation.

From our analysis of the energetic contributions to binding for each residue, we observe that there is a general trend toward the reduction of per-residue binding strength when MLN is bound to ACE2 (Figure 7). We conclude from this that the conformational disruption to the s-protein binding site when MLN is bound to ACE2 (Table S3) likely weakens key interactions between ACE2 and s-protein (Figures 6 and 7). The resulting effect is a reduction in the net ΔH_{bind} (Table 3) that is statistically significant ($p = 0.028$, $\alpha = 0.05$), although

we cannot conclude statistical significance in all of the individual per-residue energy reductions when MLN is bound to ACE2 (Figure 7). Raw data for this per-residue energy decomposition is provided in Table S5.

From Figure 7, we find additional residues that provide an enthalpic benefit to ACE2/s-protein adhesion that have not been previously identified by crystallography. For example, one residue that we find to benefit the ACE2/s-protein complex formation is the SARS-CoV-2 s-protein residue, Phe-486, which affords an enthalpic benefit to binding with ACE2 of approximately -15 kJ mol^{-1} by MM-PBSA analysis (Figure 7B). Other residues shown in Figure 7A,B show a more marginal enthalpic benefit to the complex formation, and these residues are often adjacent to the residues involved in key crystallographic interactions that are listed in Table 2. It is therefore likely that these residues, which are adjacent to known interaction pairs, may play a role in supporting the known interactions. All residues that create an enthalpic benefit to ACE2/s-protein complex formation may be valid targets for the design of novel anti-SARS-CoV-2 therapeutics.

The results illustrated in Figure 7 are congruent with results from previous work,^{20,23,24} and marginal differences are likely due to our improved sampling by MD simulation over other works and due to our choice of solute dielectric constant. Notably, the finding that the ACE2-Asp-30 to s-protein-Lys-417 interaction energetically penalizes binding through our MM-PBSA calculation (Figure 7A,B) is in contrast to previous studies where the authors state that this interaction is enthalpically beneficial.^{20,23,24} Any differences in results between those illustrated in Figure 7 and those reported in previous work are likely due to our choice of solute dielectric constant of 40, and we contend this value is the more correct choice when the solute modeled is the surface of a protein (see Methods).⁷⁶ Other authors report MM-PBSA calculations where the solute dielectric constant chosen is 1,^{20,23,24} which would change the per-residue binding enthalpy for charged or polar residues. The choice of an implicit solvation model to calculate solvation energy values (ΔH_{solv}) is useful, as doing so removes the large potential energy fluctuations from explicit water models. However, the use of implicit solvent creates

ambiguity in which parameters should be used in the continuum solvation model.

To complete the discussion of the MD simulation results, it must be noted that improved sampling of the s-protein to receptor binding/unbinding pathway would enable more reliable theoretical predictions for the development of novel therapeutics. While it has been possible to employ computational free energy methods to determine the magnitude and driving forces of the SARS-CoV-2 s-protein binding with ACE2,^{17–20,23–28} it has proven difficult to perform the binding free energy calculations reliably for such large and flexible molecular complexes, as required for future biomedical applications. Further, it is well-known that the accuracy of the computationally inexpensive end point methods that have been commonly used often depends on the value of the solute dielectric constant chosen, which can be as low as 1 or as high as 40 for the surface of a protein.^{47–49} From data in Tables 3 and S4, we can conclude that there is a desolvation penalty to the binding of s-protein with ACE2, which is consistently compensated for by the higher enthalpic benefit of the interactions in bound ACE2/s-protein complexes. From Tables S4 and 3 and Figure 6 we show that the value of ΔH_{bind} can vary considerably with MM-PBSA analysis, depending on what subset of the entire ensemble of structures is sampled in a simulation. What we can infer from the analysis presented here is that the s-protein complex with ACE2 and MLN/ACE2 is stable on a microsecond time scale and that there is a negligible shift in the heavy atom RMSD in either variant of ACE2 when s-protein binds (Tables 1 and 2). However, by our MM-PBSA analysis of binding enthalpy for systems 3 and 4, we find that the enthalpic benefit to s-protein binding is reduced for all terms defined in eq 3 when MLN is bound to ACE2 (Table 3). The reduction in the interaction stability that we observe in the presence of MLN (Table 2 and Figure 6) is likely related to the reduced enthalpic benefit to s-protein binding (Tables S4 and 3). Further to this, our analysis strongly indicated that the kinetics of s-protein binding are likely to be altered when inhibitor MLN is bound to ACE2, due to the conformational changes induced to ACE2. However, to precisely evaluate the binding strength for these protein–protein interactions, we would need to adequately account for the entropy differences between relevant states, and the full phase space between the bound and free s-protein states would need to be adequately sampled for a reliable K_{D} estimation (eq 1). This is a task that would likely require the use of enhanced sampling methods (e.g., metadynamics^{83–85}) and the incorporation of the full trimeric, virus-bound s-protein and a membrane bound ACE2 in the simulation systems.

CONCLUSION

We theoretically evaluated the effect that the binding of ACE2 active site inhibitor MLN (MLN-4760) would have on SARS-CoV-2 s-protein adhesion. The all-atom MD simulations and analyses identified the binding mode and dynamics of the experimentally established RBD of SARS-CoV-2 s-protein to ACE2 when the MLN-4760 active site inhibitor, distal from the binding interface, is present. The observed conformational changes of several regions of ACE2 induced by the bound active site inhibitor suggest that it may be possible to alter the kinetics of s-protein binding by inhibiting the ACE2 active site. Further, the observed conformational changes to the s-protein binding site of ACE2 disrupted the ACE2/s-protein inter-

actions involving the ACE2 residues Glu-35, Glu-37, Tyr-83, Lys-353, and Arg-393, thus reducing the enthalpic benefit to s-protein binding by 1.24-fold on average or by as much as 1.48-fold, as an upper limit demonstrated here. Interestingly, we observed that the ACE2-Gln-24 to s-protein-Asn-487 interaction was stabilized when MLN is bound, which suggests that this interaction pair may be targeted for a more marked reduction in s-protein binding to ACE2 with an active site inhibitor bound. On the basis of these results, we suggest that further computational and experimental studies have a strong potential to identify alternative ACE2 active site or allosteric inhibitors able to impart higher entropic and enthalpic penalties to SARS-CoV-2 s-protein adhesion by inducing a more significant conformational disorder to the ACE2 s-protein binding interface.

ASSOCIATED CONTENT

Supporting Information

The Supporting Information is available free of charge at <https://pubs.acs.org/doi/10.1021/acs.jpcb.0c11321>.

Figure S1: superimposed structures of ACE2 from PDB-ID 6M0J and ACE2 from PDB-ID 1R4L; Table S1: ensemble of ACE2 and key ACE2 motifs; Figure S2: alternate s-protein orientation for system 4; Table S2: minimum interaction distances from our initial model of the MLN/ACE2/s-protein complex and over the ensemble of structures of system 4; Figure S3: change in backbone ϕ , ψ , and ω angles of the ACE2 N-terminal; Table S3: change in the backbone ϕ , ψ , and ω angles of the residues comprising the α -1 to α -2 helices of ACE2; Table S4: MM-PBSA analysis to determine s-protein binding enthalpy values for the ACE2/s-protein complex and the MLN/ACE2/s-protein complex (PDF)

Table S5: spreadsheet containing a per residue energy decomposition for each replicate from MM-PBSA, including all ACE2 and s-protein residues (XLSX)

System 4 equilibrated: putative coordinates for the MLN-4760/ACE2/s-protein complex after NPT equilibration to 1 bar and 310 K in explicit solvent and after 400 ns of MD production simulation (ZIP)

AUTHOR INFORMATION

Corresponding Author

Irene Yarovsky – School of Engineering, RMIT University, Melbourne, Victoria 3001, Australia; orcid.org/0000-0002-4033-5150; Email: irene.yarovsky@rmit.edu.au

Authors

Billy J. Williams-Noonan – School of Engineering, RMIT University, Melbourne, Victoria 3001, Australia
Nevena Todorova – School of Engineering, RMIT University, Melbourne, Victoria 3001, Australia
Ketav Kulkarni – Department of Biochemistry and Molecular Biology, Monash University, Clayton, Victoria 3800, Australia; orcid.org/0000-0001-9965-4722
Marie-Isabel Aguilar – Department of Biochemistry and Molecular Biology, Monash University, Clayton, Victoria 3800, Australia; orcid.org/0000-0002-0234-4064

Complete contact information is available at: <https://pubs.acs.org/10.1021/acs.jpcb.0c11321>

Notes

The authors declare no competing financial interest.

ACKNOWLEDGMENTS

The authors thank Dr. Fasseli Coulibaly (Monash University, Australia) for reading the manuscript and providing useful comments. Dr. David Chalmers from the Monash Institute for Pharmaceutical Science is acknowledged for providing access to his *Silico* software package. I.Y. and M.-I.A. acknowledge the Australian Research Council for financial support under the Discovery Project scheme [DP190102290]. This research was undertaken with the assistance of resources from the National Computational Infrastructure (NCI) [NCMAS grant e87] and the HPC-GPGPU facility hosted at the University of Melbourne established with the assistance of the ARC LIEF Grant LE170100200.

REFERENCES

- (1) Gordon, D. E.; Jang, G. M.; Bouhaddou, M.; Xu, J.; Obernier, K.; White, K. M.; O'Meara, M. J.; Rezelj, V. V.; Guo, J. Z.; Swaney, D. L.; et al. A SARS-CoV-2 Protein Interaction Map Reveals Targets for Drug Repurposing. *Nature* **2020**, *583*, 459–468.
- (2) Magrone, T.; Magrone, M.; Jirillo, E. Focus on Receptors for Coronaviruses with Special Reference to Angiotensin-converting Enzyme 2 as a Potential Drug Target-A Perspective. *Endocr., Metab. Immune Disord.: Drug Targets* **2020**, *20*, 807–811.
- (3) Donoghue, M.; Hsieh, F.; Baronas, E.; Godbout, K.; Gosselin, M.; Stagliano, N.; Donovan, M.; Woolf, B.; Robison, K.; Jeyaseelan, R. A Novel Angiotensin-Converting Enzyme-Related Carboxypeptidase (ACE2) Converts Angiotensin I to Angiotensin 1–9. *Circ. Res.* **2000**, *87*, 1–9.
- (4) Tipnis, S. R.; Hooper, N. M.; Hyde, R.; Karran, E.; Christie, G.; Turner, A. J. A Human Homolog of Angiotensin-Converting Enzyme Cloning and Functional Expression as a Captopril-Insensitive Carboxypeptidase. *J. Biol. Chem.* **2000**, *275*, 33238–33243.
- (5) Turner, A. J.; Tipnis, S. R.; Guy, J. L.; Rice, G. I.; Hooper, N. M. ACEH/ACE2 is a Novel Mammalian Metalloprotease and a Homologue of Angiotensin-Converting Enzyme Insensitive to ACE Inhibitors. *Can. J. Physiol. Pharmacol.* **2002**, *80*, 346–353.
- (6) Lan, J.; Ge, J.; Yu, J.; Shan, S.; Zhou, H.; Fan, S.; Zhang, Q.; Shi, X.; Wang, Q.; Zhang, L. Structure of the SARS-CoV-2 Spike Receptor-binding Domain Bound to the ACE2 Receptor. *Nature* **2020**, *581*, 215–220.
- (7) Wang, Q.; Zhang, Y.; Wu, L.; Niu, S.; Song, C.; Zhang, Z.; Lu, G.; Qiao, C.; Hu, Y.; Yuen, K.-Y.; et al. Structural and Functional Basis of SARS-CoV-2 Entry by Using Human ACE2. *Cell* **2020**, *181*, 894–904.
- (8) Shang, J.; Ye, G.; Shi, K.; Wan, Y.; Luo, C.; Aihara, H.; Geng, Q.; Auerbach, A.; Li, F. Structural Basis of Receptor Recognition by SARS-CoV-2. *Nature* **2020**, *581*, 221–224.
- (9) Wrapp, D.; Wang, N.; Corbett, K. S.; Goldsmith, J. A.; Hsieh, C.-L.; Abiona, O.; Graham, B. S.; McLellan, J. S. Cryo-EM Structure of the 2019-nCoV Spike in the Prefusion Conformation. *Science* **2020**, *367*, 1260–1263.
- (10) Walls, A. C.; Park, Y.-J.; Tortorici, M. A.; Wall, A.; McGuire, A. T.; Velesler, D. Structure, Function, and Antigenicity of the SARS-CoV-2 Spike Glycoprotein. *Cell* **2020**, *181*, 281–292.E6.
- (11) Ou, X.; Liu, Y.; Lei, X.; Li, P.; Mi, D.; Ren, L.; Guo, L.; Guo, R.; Chen, T.; Hu, J.; et al. Characterization of Spike Glycoprotein of SARS-CoV-2 on Virus Entry and Its Immune Cross-reactivity with SARS-CoV. *Nat. Commun.* **2020**, *11*, 1620.
- (12) Clayton, D.; Hanchapola, I.; Hausler, N.; Unabia, S.; Lew, R. A.; Widdop, R. E.; Smith, A. I.; Perlmutter, P.; Aguilar, M. I. β -Amino Acid Substitution to Investigate the Recognition of Angiotensin II (AngII) by Angiotensin Converting Enzyme 2 (ACE2). *J. Mol. Recognit.* **2011**, *24*, 235–244.
- (13) Clayton, D.; Hanchapola, I.; Thomas, W. G.; Widdop, R.; Smith, A. I.; Perlmutter, P.; Aguilar, M.-I. Structural Determinants For Binding to Angiotensin Converting Enzyme 2 (ACE2) and Angiotensin Receptors. *Front. Pharmacol.* **2015**, *6*, 1–5.
- (14) Towler, P.; Staker, B.; Prasad, S. G.; Menon, S.; Tang, J.; Parsons, T.; Ryan, D.; Fisher, M.; Williams, D.; Dales, N. A.; et al. ACE2 X-Ray Structures Reveal a Large Hinge-Bending Motion Important for Inhibitor Binding and Catalysis. *J. Biol. Chem.* **2004**, *279*, 17996–8007.
- (15) Dales, N. A.; Gould, A. E.; Brown, J. A.; Calderwood, E. F.; Guan, B.; Minor, C. A.; Gavin, J. M.; Hales, P.; Kaushik, V. K.; Stewart, M.; et al. Substrate-Based Design of the First Class of Angiotensin-Converting Enzyme-Related Carboxypeptidase (ACE2) Inhibitors. *J. Am. Chem. Soc.* **2002**, *124*, 11852–11853.
- (16) Kollman, P. A.; Massova, I.; Reyes, C.; Kuhn, B.; Huo, S.; Chong, L.; Lee, M.; Lee, T.; Duan, Y.; Wang, W.; et al. Calculating Structures and Free Energies of Complex Molecules: Combining Molecular Mechanics and Continuum Models. *Acc. Chem. Res.* **2000**, *33*, 889–897.
- (17) Amin, M.; Sorour, M. K.; Kasry, A. Comparing the Binding Interactions in the Receptor Binding Domains of SARS-CoV-2 and SARS-CoV. *J. Phys. Chem. Lett.* **2020**, *11*, 4897–4900.
- (18) Saurabh, S.; Purohit, S. S. A Modified ACE2 Peptide Mimic to Block SARS-CoV2 Entry. *bioRxiv* **2020**, DOI: 10.1101/2020.05.07.082230.
- (19) García-Iriepa, C.; Hognon, C. C.; Francés-Monerris, A.; Iriepa, I.; Miclot, T.; Barone, G.; Monari, A.; Marazzi, M. Thermodynamics of the Interaction Between SARS-CoV-2 Spike Protein and Human ACE2 Receptor. Effects of Possible Ligands. *ChemRxiv* **2020**, https://chemrxiv.org/articles/preprint/Thermodynamics_of_the_Interaction_Between_SARS-CoV-2_Spike_Protein_and_Human_ACE2_Receptor_Effects_of_Possible_Ligands/12186624.
- (20) Ali, A.; Vijayan, R. Dynamics of the ACE2–SARS-CoV-2/SARS-CoV Spike Protein Interface Reveal Unique Mechanisms. *Sci. Rep.* **2020**, *10*, 14214.
- (21) Han, Y.; Kral, P. Computational Design of ACE2-Based Peptide Inhibitors of SARS-CoV-2. *ACS Nano* **2020**, *14* (4), 5143–5147.
- (22) Arantes, P. R.; Saha, A.; Palermo, G. Fighting COVID-19 Using Molecular Dynamics Simulations. *ACS Cent. Sci.* **2020**, *6*, 1654–1656.
- (23) Ghorbani, M.; Brooks, B. R.; Klauda, J. B. Critical Sequence Hotspots for Binding of Novel Coronavirus to Angiotensin Converter Enzyme as Evaluated by Molecular Simulations. *J. Phys. Chem. B* **2020**, *124*, 10034–10047.
- (24) Spinello, A.; Saltalamacchia, A.; Magistrato, A. Is the Rigidity of SARS-CoV-2 Spike Receptor-Binding Motif the Hallmark for Its Enhanced Infectivity? Insights from All-Atoms Simulations. *J. Phys. Chem. Lett.* **2020**, *11*, 4785–4790.
- (25) Hassanzadeh, K.; Perez Pena, H.; Dragotto, J.; Buccarello, L.; Iorio, F.; Pieraccini, S.; Sancini, G.; Feligioni, M. Considerations around the SARS-CoV-2 Spike Protein with Particular Attention to COVID-19 Brain Infection and Neurological Symptoms. *ACS Chem. Neurosci.* **2020**, *11*, 2361–2369.
- (26) Nguyen, H. L.; Lan, P. D.; Thai, N. Q.; Nissley, D. A.; O'Brien, E. P.; Li, M. S. Does SARS-CoV-2 Bind to Human ACE2 Stronger Than SARS-CoV? *J. Phys. Chem. B* **2020**, *124*, 7336–7347.
- (27) Zou, J.; Yin, J.; Fang, L.; Yang, M.; Wang, T.; Wu, W.; Bellucci, M.; Zhang, P. Computational Prediction of Mutational Effects on the SARS-CoV-2 Binding by Relative Free Energy Calculations. *J. Chem. Inf. Model.* **2020**, *60*, 5794–5802.
- (28) Renzi, F.; Ghersi, D. ACE2 Fragment as a Decoy for Novel SARS-CoV-2 Virus. *bioRxiv* **2020**, DOI: 10.1101/2020.04.06.028647.
- (29) Kollman, P. Free Energy Calculations: Applications to Chemical and Biochemical Phenomena. *Chem. Rev.* **1993**, *93*, 2395–2417.
- (30) Jorgensen, W. L. Free Energy Calculations: A Breakthrough for Modeling Organic Chemistry in Solution. *Acc. Chem. Res.* **1989**, *22*, 184–189.

- (31) Kollman, P. A.; Merz, K. M., Jr. Computer Modeling of the Interactions of Complex Molecules. *Acc. Chem. Res.* **1990**, *23*, 246–252.
- (32) Reynolds, C. A.; King, P. M.; Richards, W. G. Free Energy Calculations in Molecular Biophysics. *Mol. Phys.* **1992**, *76*, 251–275.
- (33) Lazaridis, T. Binding Affinity and Specificity from Computational Studies. *Curr. Org. Chem.* **2002**, *6*, 1319–1332.
- (34) Simonson, T.; Archontis, G.; Karplus, M. Free Energy Simulations Come of Age: Protein–Ligand Recognition. *Acc. Chem. Res.* **2002**, *35*, 430–437.
- (35) Brandsdal, B. O.; Österberg, F.; Almlöf, M.; Feierberg, I.; Luzhkov, V. B.; Åqvist, J. Free Energy Calculations and Ligand Binding. *Adv. Protein Chem.* **2003**, *66*, 123–158.
- (36) Foloppe, N.; Hubbard, R. Towards Predictive Ligand Design with Free-Energy Based Computational Methods? *Curr. Med. Chem.* **2006**, *13*, 3583–3608.
- (37) Mobley, D. L.; Dill, K. A. Binding of Small-Molecule Ligands to Proteins: “What you See” is not Always “What you Get. *Structure* **2009**, *17*, 489–498.
- (38) Shirts, M. R.; Mobley, D. L.; Brown, S. P. Free Energy Calculations in Structure-Based Drug Design. In *Drug Design: Structure-and Ligand-Based Approaches*; Cambridge University Press, 2010; pp 61–86.
- (39) Steinbrecher, T.; Labahn, A. Towards Accurate Free Energy Calculations in Ligand Protein-Binding Studies. *Curr. Med. Chem.* **2010**, *17*, 767–785.
- (40) Jorgensen, W. L. Efficient Drug Lead Discovery and Optimization. *Acc. Chem. Res.* **2009**, *42*, 724–733.
- (41) Merz, K. M. Limits of Free Energy Computation for Protein–Ligand Interactions. *J. Chem. Theory Comput.* **2010**, *6*, 1769–1776.
- (42) Aleksandrov, A.; Thompson, D.; Simonson, T. Alchemical Free Energy Simulations for Biological Complexes: Powerful but Temperamental... *J. Mol. Recognit.* **2010**, *23*, 117–127.
- (43) Hansen, N.; Van Gunsteren, W. F. Practical Aspects of Free-Energy Calculations: A Review. *J. Chem. Theory Comput.* **2014**, *10*, 2632–2647.
- (44) Abel, R.; Wang, L.; Mobley, D. L.; Friesner, R. A. A Critical Review of Validation, Blind Testing, and Real-World use of Alchemical Protein–Ligand Binding Free Energy Calculations. *Curr. Top. Med. Chem.* **2017**, *17*, 2577–2585.
- (45) Williams-Noonan, B. J.; Yuriev, E.; Chalmers, D. K. Free Energy Methods in Drug Design: Prospects of “Alchemical Perturbation” in Medicinal Chemistry: Miniperspective. *J. Med. Chem.* **2018**, *61*, 638–649.
- (46) Kairys, V.; Baranauskienė, L.; Kazlauskienė, M.; Matulis, D.; Kazlauskas, E. Binding Affinity in Drug Design: Experimental and Computational Techniques. *Expert Opin. Drug Discovery* **2019**, *14*, 755–768.
- (47) Wang, E.; Weng, G.; Sun, H.; Du, H.; Zhu, F.; Chen, F.; Wang, Z.; Hou, T. Assessing the Performance of the MM/PBSA and MM/GBSA methods. 10. Impacts of Enhanced Sampling and Variable Dielectric Model on Protein–Protein Interactions. *Phys. Chem. Chem. Phys.* **2019**, *21*, 18958–18969.
- (48) Wang, E.; Sun, H.; Wang, J.; Wang, Z.; Liu, H.; Zhang, J. Z. H.; Hou, T. End-Point Binding Free Energy Calculation with MM/PBSA and MM/GBSA: Strategies and Applications in Drug Design. *Chem. Rev.* **2019**, *119*, 9478–9508.
- (49) Hu, X.; Contini, A. Rescoring Virtual Screening Results with the MM-PBSA Methods: Beware of Internal Dielectric Constants. *J. Chem. Inf. Model.* **2019**, *59*, 2714–2728.
- (50) Li, F. Structural Analysis of Major Species Barriers Between Humans and Palm Civets for Severe Acute Respiratory Syndrome Coronavirus Infections. *J. Virol.* **2008**, *82*, 6984–91.
- (51) Wan, Y.; Shang, J.; Graham, R.; Baric, R. S.; Li, F. Receptor Recognition by the Novel Coronavirus from Wuhan: an Analysis Based on Decade-Long Structural Studies of SARS Coronavirus. *J. Virol.* **2020**, *94*, e00127-20.
- (52) Watanabe, Y.; Allen, J. D.; Wrapp, D.; McLellan, J. S.; Crispin, M. Site-Specific Glycan Analysis of the SARS-CoV-2 Spike. *Science* **2020**, *369*, 330–333.
- (53) Turoňová, B.; Sikora, M.; Schürmann, C.; Hagen, W. J. H.; Welsch, S.; Blanc, F. E. C.; von Bülow, S.; Gecht, M.; Bagola, K.; Hörner, C.; et al. In Situ Structural Analysis of SARS-CoV-2 Spike Reveals Flexibility Mediated by Three Hinges. *Science* **2020**, *370*, 203–208.
- (54) Casalino, L.; Gaieb, Z.; Goldsmith, J. A.; Hjorth, C. K.; Dommer, A. C.; Harbison, A. M.; Fogarty, C. A.; Barros, E. P.; Taylor, B. C.; McLellan, J. S.; et al. Beyond Shielding: The Roles of Glycans in the SARS-CoV-2 Spike Protein. *ACS Cent. Sci.* **2020**, *6*, 1722–1734.
- (55) Qiao, B.; Olvera de la Cruz, M. Enhanced Binding of SARS-CoV-2 Spike Protein to Receptor by Distal Polybasic Cleavage Sites. *ACS Nano* **2020**, *14*, 10616–10623.
- (56) Li, W.; Zhang, C.; Sui, J.; Kuhn, J. H.; Moore, M. J.; Luo, S.; Wong, S.-K.; Huang, I.-C.; Xu, K.; Vasilieva, N.; et al. Receptor and viral determinants of SARS-coronavirus adaptation to human ACE2. *EMBO J.* **2005**, *24* (8), 1634–1643.
- (57) Lu, J.; Sun, P. D. High Affinity Binding of SARS-CoV-2 Spike Protein Enhances ACE2 Carboxypeptidase Activity. *J. Biol. Chem.* **2020**, *295*, 18579–18588.
- (58) Schroedinger LLC *Maestro*; Schroedinger LLC: New York, 2016.
- (59) Bell, J.; Cao, Y.; Gunn, J.; Day, T.; Gallicchio, E.; Zhou, Z.; Levy, R.; Farid, R. *PrimeX and the Schrödinger Computational Chemistry Suite of Programs*; Schroedinger LLC: New York, 2012.
- (60) Abraham, M.; van der Spoel, D.; Lindahl, E.; Hess, B. *GROMACS user manual*, version 5.0.2; 2014; pp 1–298.
- (61) Rakhshani, H.; Dehghanian, E.; Rahati, A. Enhanced GROMACS: Toward a Better Numerical Simulation Framework. *J. Mol. Model.* **2019**, *25*, 355.
- (62) Pronk, S.; Páll, S.; Schulz, R.; Larsson, P.; Bjelkmar, P.; Apostolov, R.; Shirts, M. R.; Smith, J. C.; Kasson, P. M.; van der Spoel, D.; et al. GROMACS 4.5: A High-Throughput and Highly Parallel Open Source Molecular Simulation Toolkit. *Bioinformatics* **2013**, *29*, 845–854.
- (63) Huang, J.; MacKerell, A. D., Jr. CHARMM36 All-Atom Additive Protein Force Field: Validation Based on Comparison to NMR Data. *J. Comput. Chem.* **2013**, *34*, 2135–2145.
- (64) Lee, J.; Cheng, X.; Swails, J. M.; Yeom, M. S.; Eastman, P. K.; Lemkul, J. A.; Wei, S.; Buckner, J.; Jeong, J. C.; Qi, Y. CHARMM-GUI Input Generator for NAMD, GROMACS, AMBER, OpenMM, and CHARMM/OpenMM Simulations Using The CHARMM36 Additive Force Field. *J. Chem. Theory Comput.* **2016**, *12*, 405–413.
- (65) de Leeuw, S. W.; Perram, J. W.; Smith, E. R. Simulation of Electrostatic Systems in Periodic Boundary Conditions. I. Lattice Sums and Dielectric Constants. *Proc. Royal Soc. London A* **1980**, *373*, 27–56.
- (66) Price, D. J.; Brooks, C. L., III A Modified TIP3P Water Potential for Simulation with Ewald Summation. *J. Chem. Phys.* **2004**, *121*, 10096–10103.
- (67) Feenstra, K. A.; Hess, B.; Berendsen, H. J. Improving Efficiency of Large Time-Scale Molecular Dynamics Simulations of Hydrogen-Rich Systems. *J. Comput. Chem.* **1999**, *20*, 786–798.
- (68) Verlet, L. Computer “Experiments” on Classical Fluids. I. Thermodynamical Properties of Lennard-Jones Molecules. *Phys. Rev.* **1967**, *159*, 98.
- (69) Hess, B.; Bekker, H.; Berendsen, H. J.; Fraaije, J. G. LINCS: A Linear Constraint Solver for Molecular Simulations. *J. Comput. Chem.* **1997**, *18*, 1463–1472.
- (70) Miyamoto, S.; Kollman, P. A. Settle: An Analytical Version of the SHAKE and RATTLE Algorithm for Rigid Water Models. *J. Comput. Chem.* **1992**, *13*, 952–962.
- (71) Darden, T.; York, D.; Pedersen, L. Particle Mesh Ewald: An N. log (N) Method for Ewald Sums in Large Systems. *J. Chem. Phys.* **1993**, *98*, 10089–10092.

- (72) Bussi, G.; Donadio, D.; Parrinello, M. Canonical Sampling Through Velocity Rescaling. *J. Chem. Phys.* **2007**, *126*, No. 014101.
- (73) Parrinello, M.; Rahman, A. Crystal Structure and Pair Potentials: A Molecular-Dynamics Study. *Phys. Rev. Lett.* **1980**, *45*, 1196.
- (74) Massova, I.; Kollman, P. A. Combined Molecular Mechanical and Continuum Solvent Approach (MM-PBSA/GBSA) to Predict Ligand Binding. *Perspect. Drug Discovery Des.* **2000**, *18*, 113–135.
- (75) Kumari, R.; Kumar, R.; Open Source Drug Discovery Consortium; Lynn, A. g_mmpbsa— A GROMACS tool for high-throughput MM-PBSA calculations. *J. Chem. Inf. Model.* **2014**, *54*, 1951–1962.
- (76) Li, L.; Li, C.; Zhang, Z.; Alexov, E. On the Dielectric “Constant” of Proteins: Smooth Dielectric Function for Macromolecular Modeling and Its Implementation in DelPhi. *J. Chem. Theory Comput.* **2013**, *9*, 2126–2136.
- (77) Best, R. B.; Hummer, G. Optimized Molecular Dynamics Force Fields Applied to the Helix-Coil Transition of Polypeptides. *J. Phys. Chem. B* **2009**, *113*, 9004–9015.
- (78) Jeffrey, G. A. *An Introduction to Hydrogen Bonding*; Oxford University Press: New York, 1997; Vol. 12.
- (79) Kumar, S.; Nussinov, R. Close-Range Electrostatic Interactions in Proteins. *ChemBioChem* **2002**, *3*, 604–617.
- (80) Starr, T. N.; Greaney, A. J.; Hilton, S. K.; Crawford, K. H. D.; Navarro, M. J.; Bowen, J. E.; Tortorici, M. A.; Walls, A. C.; Veesler, D.; Bloom, J. D. Deep Mutational Scanning of SARS-CoV-2 Receptor Binding Domain Reveals Constraints on Folding and ACE2 Binding. *Cell* **2020**, *182*, 1295–1310.e20.
- (81) Sun, H.; Li, Y.; Shen, M.; Tian, S.; Xu, L.; Pan, P.; Guan, Y.; Hou, T. Assessing the Performance of MM/PBSA and MM/GBSA Methods. 5. Improved Docking Performance Using High Solute Dielectric Constant MM/GBSA and MM/PBSA Rescoring. *Phys. Chem. Chem. Phys.* **2014**, *16*, 22035–22045.
- (82) Chen, F.; Liu, H.; Sun, H.; Pan, P.; Li, Y.; Li, D.; Hou, T. Assessing the Performance of the MM/PBSA and MM/GBSA Methods. 6. Capability to Predict Protein–Protein Binding Free Energies and Re-rank Binding Poses Generated by Protein–Protein Docking. *Phys. Chem. Chem. Phys.* **2016**, *18*, 22129–22139.
- (83) Barducci, A.; Bussi, G.; Parrinello, M. Well-Tempered Metadynamics: A Smoothly Converging and Tunable Free-Energy Method. *Phys. Rev. Lett.* **2008**, *100*, No. 020603.
- (84) Bonomi, M.; Barducci, A.; Parrinello, M. Reconstructing the Equilibrium Boltzmann Distribution from Well-Tempered Metadynamics. *J. Comput. Chem.* **2009**, *30*, 1615–1621.
- (85) Bussi, G.; Laio, A. Using Metadynamics to Explore Complex Free-Energy Landscapes. *Nature Rev. Phys.* **2020**, *2*, 200–212.